MIT Open Access Articles

DISCREPANT MASS ESTIMATES IN THE CLUSTER OF GALAXIES ABELL 1689

DISCREPANT MASS ESTIMATES IN THE CLUSTER OF GALAXIES ABELL 1689

E.-H. PENG[1], K. ANDERSSON[1], M. W. BAUTZ[1], AND G. P. GARMIRE[2]
[1] MKI, Massachusetts Institute of Technology, Cambridge, MA 02139, USA; epeng@mit.edu
[2] Department of Astronomy and Astrophysics, Pennsylvania State University, PA 16802, USA

ABSTRACT

We present a new mass estimate of a well studied gravitational lensing cluster, Abell 1689, from deep *Chandra* observations with a total exposure of 200 ks. Within $r = 200\,h^{-1}$ kpc, the X-ray mass estimate is systematically lower than that of lensing by 30%–50%. At $r > 200\,h^{-1}$ kpc, the mass density profiles from X-ray and weak lensing methods give consistent results. The most recent weak lensing work suggests a steeper profile than what is found from the X-ray analysis, while still in agreement with the mass at large radii. Fitting the total mass profile to a Navarro–Frenk–White model, we find $M_{200} = (1.16^{+0.45}_{-0.27}) \times 10^{15}\,h^{-1}\,M_\odot$ with a concentration, $c_{200} = 5.3^{+1.3}_{-1.2}$, using nonparametric mass modeling. With parametric profile modeling, we find $M_{200} = (0.94^{+0.11}_{-0.06}) \times 10^{15}\,h^{-1}\,M_\odot$ and $c_{200} = 6.6^{+0.4}_{-0.4}$. This is much lower compared to masses deduced from the combined strong and weak lensing analysis. Previous studies have suggested that cooler small-scale structures can bias X-ray temperature measurements or that the northern part of the cluster is disturbed. We find these scenarios unlikely to resolve the central mass discrepancy since the former requires 70%–90% of the space to be occupied by these cool structures, and excluding the northern substructure does not significantly affect the total mass profiles. A more plausible explanation is a projection effect. Assuming that the gas temperature and density profiles have a prolate symmetry, we can bring the X-ray mass estimate into a closer agreement with that of lensing. We also find that the previously reported high hard-band to broadband temperature ratio in A1689, and many other clusters observed with *Chandra*, may be resulting from the instrumental absorption that decreases 10%–15% of the effective area at ∼1.75 keV. Caution must be taken when analyzing multiple spectral components under this calibration uncertainty.

Key words: galaxies: clusters: individual (Abell 1689) – X-rays: galaxies: clusters

Online-only material: color figures

1. INTRODUCTION

Abell 1689 is a massive galaxy cluster with the largest known Einstein radius to date, $\theta_E = 45''$ for $z_s = 1$ (e.g., Tyson et al. 1990; Miralda-Escude & Babul 1995; Broadhurst et al. 2005a, 2005b), located at a moderately low redshift of $z = 0.187$ (Frye et al. 2007). It has a regular X-ray morphology, indicating that the cluster is likely in hydrostatic equilibrium, but the mass derived from the X-ray measurement is often a factor of 2 or more lower than that from gravitational lensing at most radii. Using *XMM-Newton* observations, Andersson & Madejski (2004, hereafter A04) find an asymmetric temperature distribution and a high-redshift structure in A1689, providing evidence for an ongoing merger in this cluster.

Saha et al. (2007) confirm the existence of substructures, using different sets of lensed images. This is also seen in other lensing work (e.g., Broadhurst et al. 2005b; Diego et al. 2005; Zekser et al. 2006; Halkola et al. 2006; Limousin et al. 2007). Though these clumps are clearly identified, they only contribute $\simeq 7\%$ of the total mass within $250\,h^{-1}$ kpc and are likely to be line-of-sight filaments rather than distinct merging groups. Furthermore, Łokas et al. (2006) used the redshift distribution of galaxies to conclude that A1689 is probably surrounded by a few structures superposed along the line of sight that do not interact with the cluster dynamically, but would affect lensing mass estimates.

A recent joint *Chandra*, *Hubble Space Telescope* (*HST*)/ACS, and Subaru/Suprime cam analysis by Lemze et al. (2008a, hereafter L08) suggested that the temperature of A1689 could be as high as $T = 18$ keV at $100\,h^{-1}$ kpc, almost twice as large as the observed value at that radius. The derived three-

dimensional temperature profile was based on the X-ray surface brightness, the lensing shear, and the assumption of hydrostatic equilibrium. From the disagreement between the observed X-ray temperature and the deduced one, Lemze et al. (2008a) concluded that denser, colder, and more luminous small-scale structures could bias the X-ray temperature.

In another study of 192 clusters of galaxies from the *Chandra* archive, Cavagnolo et al. (2008) find a very high hard-band $(2/(1 + z) - 7\text{ keV})$ to broad-band (0.7–7 keV) temperature ratio for A1689, $1.36^{+0.14}_{-0.12}$ compared to 1.16 ± 0.10 for the whole sample. They also find that merging clusters tend to have a higher temperature ratio, as predicted by Mathiesen & Evrard (2001) where this high ratio is attributed to accreting cool subclusters lowering the broadband temperature by contributing large amounts of line emission in the soft band. The hard-band temperature, however, should be unaltered by this emission. The simulations of Mathiesen & Evrard (2001) show an increase of temperature ratios of ∼20% in general, which is close to the average of the sample of Cavagnolo et al. (2008), 16%.

A recent study, using the latest *Chandra* data (Riemer-Sørensen et al. 2009), claims that the cluster harbors a cool core and thus is relaxed based on a hardness-ratio map analysis. They further calculate a mass profile from the X-ray data and conclude that the X-ray and lensing measurements are in good agreement when the substructure to the northeast is excluded.

In this work, we examine the possibility of an extra spectral component in the X-ray data and derive an improved gravitational mass profile, including a recent 150 ks *Chandra* observation. Section 2 describes the details of data reduction and examines the possibility of an uncorrected absorption edge in the data. In Section 3, we explore the physical properties of

the potential cool substructures under a two-temperature (2T) model and examine if they can be used to explain the high hardband to broadband temperature ratio. In Section 4, assuming that the temperature profile derived by Lemze et al. (2008a) is real, we investigate what this implies for the required additional cool component. In Section 5, we derive the mass profile under both one- and two-temperature-phase assumptions, using both parametric and nonparametric methods. Finally, we discuss our results in Section 6 and summarize in Section 7.

Throughout this paper, we assume $H_0 = 100\,h^{-1}$ km s^{-1} Mpc^{-1}, $\Omega_m = 0.3$, and $\Omega_\lambda = 0.7$, which gives $1'' = 2.19\,h^{-1}$ kpc at the cluster redshift of 0.187 (Frye et al. 2007). Abundances are relative to the photospheric solar abundances of Anders & Grevesse (1989). All errors are 1σ unless otherwise stated.

2. DATA REDUCTION

2.1. Chandra

Chandra data were processed through CIAO 4.0.1 with CALDB 3.4.3. Since all of the observations had gone through Repro III in the archive, reprocessing data was not needed. Updated charge-transfer inefficiency and time-dependent gain corrections had already been applied. For data taken in VFAINT telemetry mode, additional screening to reject particle background was used. Events with bad CCD columns and bad grades were removed. Light curves were extracted from four I-chips with cluster core and point sources masked in the 0.3–12 keV band and filtered by *lc_clean* which used 3σ clipping and a cut at 20% above the mean. Finally, *make_readout_bg* were used to generated Out-of-Time event file. These events were multiplied by 1.3% and subtracted from the images or the spectra to correct read-out artifacts. For spectral analysis, emission-weighted response matrices and effective area files were constructed for each spectral region by *mkacisrmf* and *mkwarf*.

2.2. Background Subtraction and Modeling

Blank-field data sets[3] were used to estimate the background level. After reprojecting the blank-sky data sets onto the cluster's sky position, the background was scaled by the count rate ratio between the data and the blank-field background in the 9.5–12 keV band to account for the variation of particle-induced background. Below 1 keV, the spatial varying galactic ISM emission (Markevitch et al. 2003) could cause a mismatch between the real background and the blank-field data. By analyzing the spectra in the same field but sufficiently far from the cluster, tailoring this soft component can be made using an unabsorbed $T \sim 0.2$ keV, solar abundance thermal model (Vikhlinin et al. 2005).

The current available blank-sky data were created from observations before 2005. As the solar cycle gradually reaches its minimum, the particle-induced background increases. Therefore, newer observations need a much higher background normalization with a factor of 1.2–1.3. This leads an overestimate of the background in the soft band because other components like cosmic X-ray background (CXB) does not change as the particle-induced background does. To correct the oversubtracted CXB and halo emission, an absorbed power law with photon index fixed at 1.4 (De Luca & Molendi 2004) plus an unabsorbed thermal model was used to fit the blank-field background-subtracted spectrum taken at $r > 13'$.

The background normalization factors used for each observation are listed in Table 1.

3 http://asc.harvard.edu/cal/Acis/Cal_prods/bkgrnd/acisbg

Table 1
Chandra Observation Log

| ObsID	Data Mode	Obs. Date (yyyy-mm-dd)	Exposure (ks)	Background Normalization			
				I0	I1	I2	I3
540	FAINT	2000-04-15	10.3	1.06	1.09	1.03	1.11
1663	FAINT	2001-01-07	10.7	1.00	0.98	0.99	1.04
5004	VFAINT	2004-02-28	19.9	0.93	0.89	0.89	0.94
6930	VFAINT	2006-03-06	75.9	1.21	1.18	1.18	1.28
7289	VFAINT	2006-03-09	74.6	1.19	1.20	1.19	1.27

2.3. XMM-Newton

The data from two MOS detectors were processed with the XMMSAS 6.1.0 tool, *emchain*. Background flares were removed by a double-filtering method (Nevalainen et al. 2005) from $E > 10$ keV and 1–5 keV light curves. Only events with pixel PATTERNs 0–12 were selected. Since *XMM-Newton* data were only used to crosscheck the result of the multi-component analysis of *Chandra* spectra, extracted from the central region where background modeling is relatively unimportant, we used the simpler local background, taken from $6'$ to $8'$. Spectral response files were created by *rmfgen* and *arfgen*. We did not include PN data because the measured mean redshift, 0.169 ± 0.001, was not consistent with those from *XMM-Newton* MOS or *Chandra* data. This could indicate a possible gain offset for PN detector, although Andersson & Madejski (2004) did not find any evidence for that.

2.4. Systematic Uncertainties

Lemze et al. (2008a) pointed out some issues about previous *Chandra* observations (ObsID 540, 1663, and 5004). The column density from *Chandra* data is much lower than the Galactic value, 1.8×10^{20} cm^{-2} (Dickey & Lockman 1990), which is also supported by the *ROSAT* data (Andersson & Madejski 2004). The temperature difference can be as high as 1.3 keV depending on the choice of column density. In the high-energy band, the data are systematically higher than the model prediction. With two long *Chandra* observations, ObsID 6930 and 7289, we clearly see an unusual feature in the data sets which may give clues to problems mentioned before. Figure 1 shows an absorbed APEC model (Smith et al. 2001) fitted to the central $3'$ spectrum. The prominent residual at ~ 1.75 keV is present in all of our observations and appeared as the biggest contributor to the total χ^2 (see Figure 2). This residual cannot be eliminated by adjusting individual abundances in the cluster or in the absorbing column (the cluster is at high galactic latitude). Because the residual around 1.75 keV is an order of magnitude larger than the background, it is not likely related to the background subtraction. In addition to this absorption, the residuals are systematically rising with the energy from negative to positive values. This trend is not changed when fitting the spectrum with data between 1.7 and 2.0 keV excluded (Figure 2). We found that multiplying an XSPEC Edge model can correct the residual at ~ 1.75 keV, remove steadily rising residuals with the energy, and make the column density agree with the Galactic value.
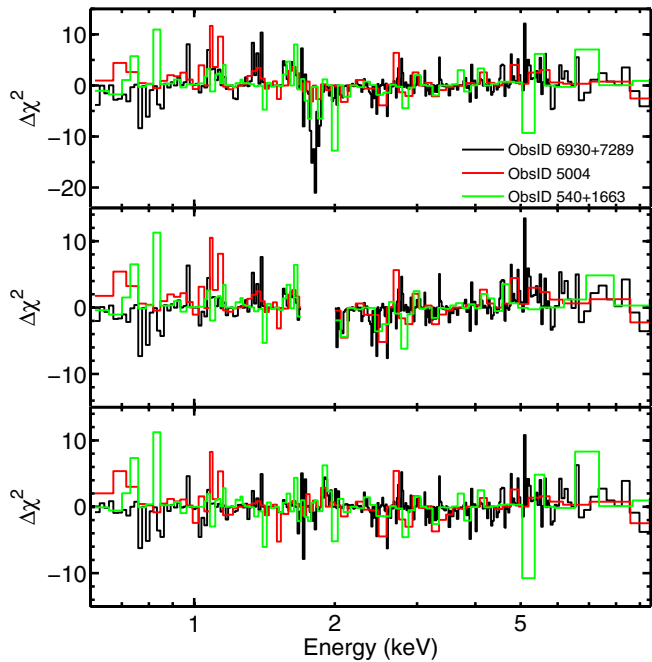
Since the spectrum was extracted from a very large region, we averaged the position-dependent response matrices and effective area functions by the number of counts at each location. It is possible that the absorption feature is caused by improper weighting of those response files, or that this
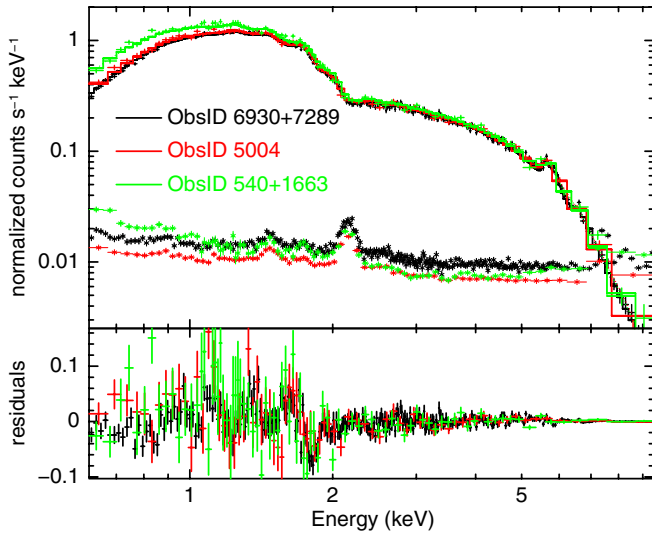
Figure 1. 0.6–9.5 keV *Chandra* spectrum of A1689 from the central 3′ region. The upper panel shows the data, plotted against an absorbed VAPEC model (solid line) with each element's abundance and absorption column density as free parameters. The lower panel shows residuals.

(A color version of this figure is available in the online journal.)

Figure 2. Fit residuals, showing each channel's contribution to the total χ^2. Top: an absorbed VAPEC model fit to central 3′ spectrum. Middle: the same as above, ignoring data in 1.7–2 keV. Bottom: adding an absorption edge with $E_{\mathrm{thresh}} = 1.77$ keV and $\tau = 0.12$.

(A color version of this figure is available in the online journal.)

Table 2
Absorption Edge Parameters

Model	Fit Range	E_{thresh} (keV)	τ
1T	$2.'5 \times 2.'5$	$1.75^{+0.01}_{-0.01}$	$0.15^{+0.01}_{-0.01}$
1T	$r < 3'$	$1.74^{+0.01}_{-0.01}$	$0.14^{+0.01}_{-0.01}$
1T	$r < 3'$, ignore 1.75–1.85 keV	$1.76^{+0.03}_{-0.02}$	$0.13^{+0.01}_{-0.01}$
2T[a]	$r < 3'$, ignore 1.75–1.85 keV	$1.76^{+0.06}_{-0.02}$	$0.12^{+0.02}_{-0.01}$
1T+PL[b]	$r < 3'$, ignore 1.75–1.85 keV	$1.76^{+0.03}_{-0.02}$	$0.11^{+0.01}_{-0.01}$
1T	$0.'2 < r < 3'$	$1.74^{+0.01}_{-0.01}$	$0.14^{+0.01}_{-0.01}$
1T	$0.'2 < r < 3'$, ignore 1.75–1.85 keV	$1.90^{+0.04}_{-0.06}$	$0.12^{+0.01}_{-0.01}$

Notes.
[a] $T_1 = 8.0^{+0.5}_{-0.5}$ keV, $T_2 = 34^{+12}_{-6}$ keV.
[b] $T_1 = 9.3^{+0.3}_{-0.4}$ keV, $\Gamma = -0.7^{+0.3}_{-0.4}$.
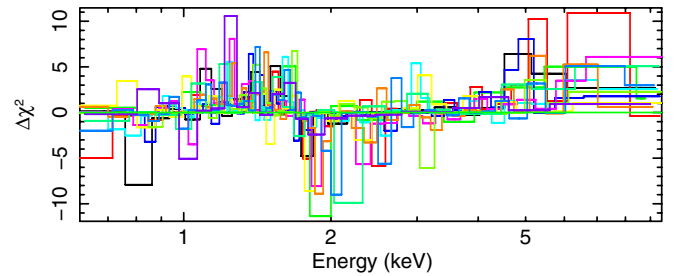
Figure 3. Residuals from an absorbed APEC model fitted to 12 spectra extracted from the central $2.'5 \times 2.'5$ region of ObsID 6930 and 7289. We simultaneously fit these spectra and tied all parameters, except the normalization, together.

(A color version of this figure is available in the online journal.)

the column density, $(1.0^{+0.4}_{-0.4}) \times 10^{20}$ cm^{-2} (90% confidence level), appears low. When adding an absorption edge to the single-temperature model, the derived parameters of this edge, $E_{\mathrm{thresh}} = 1.75^{+0.01}_{-0.01}$ keV and $\tau = 0.15^{+0.01}_{-0.01}$, are consistent with results from the integrated spectrum. In fact, E_{thresh} and τ do not strongly depend on how we model the cluster spectrum. We list fitted values of E_{thresh} and τ from different cluster models and spectral extraction regions in Table 2. Similar values are also found in other *Chandra* data sets (see the Appendix).

The low column density can be explained by the absorption at ~1.75 keV. This absorption has to be something like an edge, which affects the wide energy range of the spectrum, rather than an absorption line that influences only a limited energy range. The consequence to the fit resulting from this absorption is that the overall spectral normalization decreases. Since less soft photons are produced from the model, the heavy absorption by the foreground is no longer needed. We quantified the above statement in Table 3 in which we simulated 100 single-temperature spectra with an absorption edge at $E_{\mathrm{thresh}} = 1.74$ keV and $\tau = 0.14$, fit with a single-temperature (1T) model, and compared with the observations. The spectral normalization is increasing with rising column density as we exclude more data around 1.75 keV. Meanwhile, the cluster temperature and abundance are slightly decreasing. The changes of those parameters from different bandpass used in the fitting match perfectly to what are seen in the real data.

The CCD calibration around the Si-edge for ACIS-I detectors is a known issue (N. Schulz 2008, private communication). However, it is unknown whether a correction like an edge

peculiarity only exists at certain regions. To dispel those doubts, we separated the central $2.'5 \times 2.'5$ area into 12 square regions and simultaneously fit these spectra with one spectral model (we only used data from ObsID 6930 and 7289 to simplify the fitting procedure). All parameters, except for the normalization, were tied together. The residuals from the single-temperature fit are shown in Figure 3. Although the fit is now acceptable with a $\chi^2/\mathrm{dof} = 3448.8/3387$, the residuals still show the same systematic trend as seen in the composite spectrum, and

Table 3
Summary of $r < 3'$ Spectral Fits and 1T Simulations

Fit Range	Chandra Observations					Simulated 200 ks Spectra[a]			
	T (keV)	Z ($Z_\odot$)	N_H (10^{20} cm^{-2})	Norm (10^{-2})	χ^2/dof	T (keV)	Z ($Z_\odot$)	N_H (10^{20} cm^{-2})	Norm (10^{-2})
0.6–9.5 keV[b]	$10.5^{+0.1}_{-0.1}$	$0.36^{+0.02}_{-0.02}$	$1.9^{+0.2}_{-0.2}$	$1.920^{+0.007}_{-0.007}$	1591/1390	$10.4^{+0.1}_{-0.1}$	$0.36^{+0.02}_{-0.02}$	$1.9^{+0.1}_{-0.2}$	$1.899^{+0.008}_{-0.006}$
0.6–9.5 keV	$10.7^{+0.4}_{-0.1}$	$0.41^{+0.02}_{-0.02}$	$0.7^{+0.2}_{-0.2}$	$1.841^{+0.007}_{-0.007}$	1867/1390	$10.6^{+0.1}_{-0.1}$	$0.40^{+0.02}_{-0.02}$	$0.6^{+0.1}_{-0.2}$	$1.820^{+0.008}_{-0.007}$
Ignore 1.75–1.85 keV	$10.6^{+0.1}_{-0.1}$	$0.40^{+0.02}_{-0.02}$	$0.9^{+0.2}_{-0.2}$	$1.857^{+0.007}_{-0.007}$	1743/1366	$10.5^{+0.1}_{-0.1}$	$0.39^{+0.02}_{-0.02}$	$0.8^{+0.1}_{-0.1}$	$1.833^{+0.008}_{-0.006}$
Ignore 1.7–2.0 keV	$10.5^{+0.1}_{-0.1}$	$0.39^{+0.02}_{-0.02}$	$1.1^{+0.2}_{-0.2}$	$1.868^{+0.008}_{-0.008}$	1645/1327	$10.3^{+0.1}_{-0.1}$	$0.38^{+0.02}_{-0.02}$	$1.2^{+0.2}_{-0.1}$	$1.852^{+0.008}_{-0.007}$
Ignore 1.7–2.5 keV	$10.4^{+0.1}_{-0.1}$	$0.38^{+0.02}_{-0.02}$	$1.6^{+0.2}_{-0.2}$	$1.892^{+0.008}_{-0.008}$	1466/1222	$10.2^{+0.1}_{-0.1}$	$0.37^{+0.02}_{-0.01}$	$1.6^{+0.2}_{-0.2}$	$1.877^{+0.007}_{-0.008}$
Ignore 1.7–3.0 keV	$10.4^{+0.1}_{-0.1}$	$0.37^{+0.02}_{-0.02}$	$1.8^{+0.2}_{-0.2}$	$1.904^{+0.009}_{-0.009}$	1317/1120	$10.2^{+0.1}_{-0.1}$	$0.36^{+0.02}_{-0.01}$	$1.7^{+0.2}_{-0.2}$	$1.886^{+0.008}_{-0.009}$
1.7–7.0 keV	$13.1^{+0.3}_{-0.3}$	$0.44^{+0.02}_{-0.02}$	1.8	$1.817^{+0.008}_{-0.008}$	1100/960	$12.7^{+0.3}_{-0.3}$	$0.44^{+0.02}_{-0.02}$	1.8	$1.790^{+0.008}_{-0.008}$
0.7–7.0 keV	$10.1^{+0.1}_{-0.1}$	$0.40^{+0.02}_{-0.02}$	1.8	$1.867^{+0.006}_{-0.006}$	1655/1164	$10.0^{+0.1}_{-0.1}$	$0.39^{+0.02}_{-0.02}$	1.8	$1.849^{+0.005}_{-0.006}$

Notes. Errors are 1σ or 68% CL for 100 simulations.
[a] The absorption edge is at $E_{\rm thresh} = 1.74$ keV with $\tau = 0.14$. We used $T = 10.5$ keV, $Z = 0.36~Z_\odot$, $z = 0.187$, Norm $= 1.9 \times 10^{-2}$ (corresponding to $S_{X[0.6–9.5\,{\rm keV}]} = 2.4 \times 10^{-11}$ erg cm^{-2} s^{-1}), and $N_H = 1.8 \times 10^{20}$ cm^{-2}.
[b] Multiplied by an absorption edge at $E_{\rm thresh} = 1.74$ keV with $\tau = 0.14$.

model is needed, or if we should simply ignore the data around the Si edge. If the former is true, results from the multiple-component analysis or the hard-band/broadband temperature measurement without applying this edge model beforehand are very questionable. As seen in Table 3, including the edge model can make the hard-band temperature 30% hotter than that of the broad band. This temperature ratio depends on the cluster temperature and the quality of the data. On the other hand, if the latter is true, the spectrum implies that an additional component which is much harder than 10 keV emission is definitely required. Though, the fit is not as good as that with an edge model. From the fact that the absorption depth is sufficiently far from the zero, even if we exclude data around 1.75 keV (Table 2), the intensity jump around this energy indeed exists.

A1689 is a very hot cluster that unfortunately will be seriously affected by the calibration uncertainty around the Si edge if that can be modeled by something similar to an edge model. Lacking the knowledge that correctly treats the systematic residuals seen in the data, we provide both models, applying an absorption edge or simply ignoring the data around 1.75 keV, as our best guess to the thermal state of this cluster.

2.5. Spectral Fitting

Spectra were fitted with XSPEC 12.3.1 package (Arnaud 1996). We adopted χ^2 statistic and grouped the spectra to have a minimum of 25 counts per bin. However, when fitting background-dominated spectra, χ^2 statistic is proven to give biased temperature (Leccardi & Molendi 2007). Another choice available in XSPEC is using Cash statistic with modeled, rather than subtracted background. Since modeling the background needs many components: cosmic-ray-induced background (broken power laws plus several Gaussians), particle background (broken power laws), cosmic X-ray background (power law), galactic emission (thermal), etc., the whole spectral model will be very complicated for analysis like deprojection, which simultaneously fits all of the spectra extracted at different radii. We decided to use χ^2 statistic but with a different grouping method to bypass the difficulty in background modeling.

As shown in Table 4, we simulated 500 Chandra spectra with $N_H = 1.8 \times 10^{20}$ cm^{-2}, $Z = 0.2$ solar, and $T = 9, 7, 5$ keV

Table 4
Summary of 1T Simulations of 150 ks Chandra Spectra at $r = 6\farcm5$–$8\farcm8$

Min Counts (1)	T_0 (keV) (2)	$T_{\rm med}$ (keV) (3)	dof$_{\rm mean}$ (4)
25 (tot)	9	$4.9^{+2.1}_{-1.2}$	396
	7	$4.2^{+1.6}_{-1.1}$	396
	5	$3.4^{+0.9}_{-0.7}$	395
100 (tot)	9	$6.8^{+5.1}_{-1.8}$	142
	7	$5.9^{+3.1}_{-1.7}$	142
	5	$4.3^{+1.5}_{-1.1}$	141
400 (tot)	9	$7.9^{+7.2}_{-2.4}$	40
	7	$6.6^{+4.2}_{-2.0}$	40
	5	$4.8^{+1.9}_{-1.3}$	40
2 (net)	9	$8.6^{+7.8}_{-2.7}$	170
	7	$7.2^{+4.7}_{-2.2}$	166
	5	$5.2^{+1.9}_{-1.4}$	155

Notes. (1) Minimum (total or net) counts per channel, (2) input temperature, (3) median temperature, (4) median dof. Errors are 68% CL for 500 simulations.

with Norm[4] $= 1.51 \times 10^4$, 1.52×10^4, 1.56×10^4, respectively. The spectral normalization was chosen to match the observed flux at $r = 6\farcm5$–$8\farcm8$, where the background is $\sim$90% of the source in 0.9–7.0 keV band. Spectra were generated based on the response files of ObsID 6930 and 7289 with a total exposure time of 150 ks. When data are binned to have a minimum of 25 total counts (background included) per channel, a 9 keV gas will be measured to be 5 keV. Raising the threshold can lessen this bias. However, even with 400 counts per bin, which greatly reduces the spectral resolution by a factor of 10, the temperature is still being underestimated by $\sim$1 keV for $T = 9$ keV gas. We found out that binning data to have at least 2 counts above the background can recover the true temperature, though this minimum has to be adjusted according to the background contribution. Spectra at large radii were binned by this grouping scheme.

---

[4] Spectral normalization, Norm $= \frac{10^{-14}}{4\pi((1+z)D_A)^2} \int n_e n_H dV$, where n_e and n_H are in cm^{-3}, V in cm^3, and D_A in cm.

Table 5
Best-fit VAPEC Parameters

Instrument	T (keV)	z	Ne	Mg	Si	S	Ar	Ca	Fe	Ni	χ^2/dof
Chandra[a]	$10.2^{+0.1}_{-0.1}$	$0.186^{+0.001}_{-0.001}$	$0.59^{+0.32}_{-0.29}$	$1.95^{+0.30}_{-0.30}$	0.4_f	< 0.05	< 0.19	< 0.12	$0.40^{+0.02}_{-0.02}$	$3.60^{+0.44}_{-0.47}$	1664/1360
Chandra[b]	$10.5^{+0.1}_{-0.1}$	$0.186^{+0.001}_{-0.001}$	< 0.18	$1.16^{+0.22}_{-0.42}$	0.4_f	$0.66^{+0.22}_{-0.32}$	< 0.38	< 0.09	$0.37^{+0.01}_{-0.02}$	$2.77^{+0.48}_{-0.45}$	1545/1382
XMM-Newton MOS	$9.4^{+0.1}_{-0.1}$	$0.183^{+0.001}_{-0.001}$	$0.35^{+0.40}_{-0.35}$	$1.55^{+0.43}_{-0.40}$	$0.50^{+0.20}_{-0.19}$	$0.64^{+0.23}_{-0.23}$	< 0.57	$1.38^{+0.69}_{-0.71}$	$0.31^{+0.02}_{-0.02}$	$0.57^{+0.49}_{-0.47}$	982/840

Notes. Al, O fixed at 0.4 solar and He, C, N at 1 solar. For the elements whose abundances reach the lower bound, zero, only the upper limits are shown. Errors are 1σ.
[a] Without an absorption edge and ignoring data at 1.75–1.85 keV.
[b] With an absorption edge. Edge parameters are determined from the data with $E_{\mathrm{thresh}} = 1.74^{+0.01}_{-0.01}$ keV and $\tau = 0.13^{+0.01}_{-0.01}$.

3. SPECTRAL ANALYSIS

3.1. Single-temperature Model

We first determined the general properties of the cluster, using the spectrum extracted from the central $3'$ ($395\, h^{-1}$ kpc) region and fitting it with a single-temperature VAPEC model. The Ne, Mg, Si, S, Ar, Ca, Fe, Ni abundances and the redshift were free to vary. The column density was fixed at the Galactic value. The best-fit parameters are listed in Table 5. For *Chandra* data, we fixed the Si abundance at 0.4 $Z_\odot$, since the residual at 1.75 keV (Section 2.4) was close to Si xiv Kα line (2.01 keV, rest frame).

Table 5 shows that a single-temperature model is moderately adequate for *XMM-Newton* MOS data but not for *Chandra* when the absorption edge is not modeled. In addition to this difference, the *Chandra* temperature is ∼1 keV higher than that of *XMM-Newton*. This temperature disagreement is likely related to the cross-calibration problems, as noted in other studies (e.g., Kotov & Vikhlinin 2005; Vikhlinin et al. 2006; Snowden et al. 2008; L. David[5]), but it could also be caused by incorrect cluster modeling. A two-temperature model will be investigated in Section 3.2.

Chandra data also have a higher Fe and a much higher Ni abundance, resulting an unusually high Ni/Fe ratio of 7.5 ± 1.3 and 9.0 ± 1.2 Ni$_\odot$/Fe$_\odot$ with and without an absorption edge correction, respectively, in contrast to the *XMM-Newton* value of 1.8 ± 1.6 Ni$_\odot$/Fe$_\odot$. Our *XMM-Newton* MOS result is in agreement with that of de Plaa et al. (2007), 0.9 ± 1.5 Ni$_\odot$/Fe$_\odot$, obtained from MOS and PN spectra from the $r < 1.'3$ region with a differential emission measure MEKAL-based model, *wdem* (Kaastra et al. 2004). Such a high Ni/Fe ratio greatly exceeds the yield of typical SN Ia models (Iwamoto et al. 1999), which range from 1.4 to 4.8 Ni$_\odot$/Fe$_\odot$. Since there is a known temperature discrepancy between *Chandra* and *XMM-Newton* that would affect elemental abundance determinations, direct Fe and Ni line measurements will be conducted in Section 3.4.

The S abundance, determined mostly by the S xvi Kα line at 2.62 keV (rest frame), should be accurately measured for *XMM-Newton* EPIC since it suffers little systematic uncertainty (Werner et al. 2008). However, without an absorption edge correction, there is basically no S detection for *Chandra* data, which strongly contradicts the *XMM-Newton* result. This shows the great impact of the absorption at 1.75 keV. When including an edge model into the fit, we have consistent S abundances for both instruments.

3.2. Two-temperature Model

To get some clues to the nature of the claimed cool substructures in A1689, a simple two-temperature model was fitted to

the spectrum extracted from the $r < 3'$ ($395\, h^{-1}$ kpc) region where the quality of the data was high enough to test it. We used two absorbed VAPEC models, with variable normalization but linked metallicities between the two phases. The column density was fixed at the Galactic value. To reduce the uncertainty on measuring metallicities, we tied the abundances of α-elements (O, Ne, Mg, Si, S, Ar, and Ca) together and fixed the remaining abundances at the solar value, except for Fe and Ni. Since the hotter phase temperature, T_{hot}, was harder to constrain, it was frozen at a certain value above the best-fit single-temperature fit, T_{1T}. We changed this increment from 0.5 to 50 keV to explore the whole parameter space.
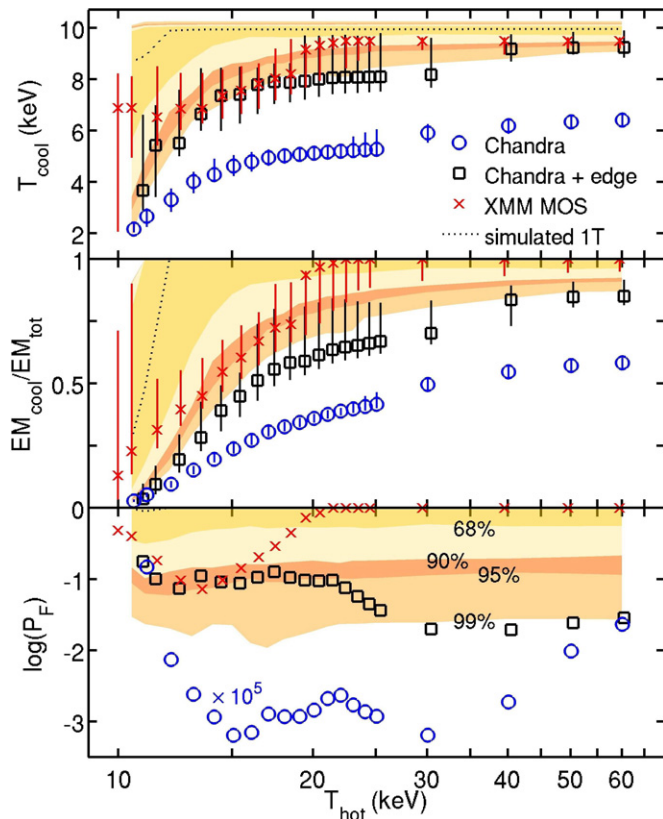
Figure 4 shows the temperature of the cooler gas, T_{cool}, and the fractional contribution of the cooler gas, EM$_{\mathrm{cool}}$/EM$_{\mathrm{total}}$, as a function of T_{hot}. As T_{hot} increases, T_{cool} and EM$_{\mathrm{cool}}$/EM$_{\mathrm{total}}$ increase as well. T_{cool} eventually becomes T_{1T} once T_{hot} is greater than 20 keV and very little gas is left in the hot phase, which is also supported by the *XMM-Newton* data. For $T_{\mathrm{hot}} \approx$ 18 keV, there has to be 30%, 60% of the cool gas at the temperature of 5, 8 keV inferred from *Chandra* and *XMM-Newton* data, respectively. *Chandra* absorption corrected data show similar results as *XMM-Newton* data do at this temperature. Although there is some inconsistency between *Chandra* and *XMM-Newton* data, both indicate that the cool component, if it indeed exists, is not cool at all. $T = 5$ keV is the typical temperature of a medium-sized cluster with a mass of $M_{500} = 2.9 \times 10^{14} h^{-1}\, M_\odot$ (Vikhlinin et al. 2006).

To quantify how significant the detection of this extra component was, we conducted an *F*-test from the fits of 1T (the null model) and 2T models. However, because the 2T model reduces to 1T when the normalization of one of the two components hits the parameter space boundary (i.e., zero), the assumption of *F*-test is not satisfied (see Protassov et al. 2002). Therefore, we simulated 1000 1T *Chandra* spectra and performed the same procedure to derive the *F*-test probability, P_F, based on the *F*-distribution. Figure 4 shows the distribution of P_F from simulated data at the 68, 90, 95, and 99 percentile overplotted with P_F from *Chandra* and *XMM-Newton* data. We plot P_F in Figure 4 rather than the *F*-statistic, since P_F is a scalar that does not depend on the degrees of freedom of the fits and is ideal to compare observations that have different data bins. For $T_{\mathrm{hot}} < 20$ keV, both the edge-corrected *Chandra* data and the *XMM-Newton* data are within the 95 percentile of the simulated 1T model and we conclude that a 2T model is possible but not necessary to describe the data.

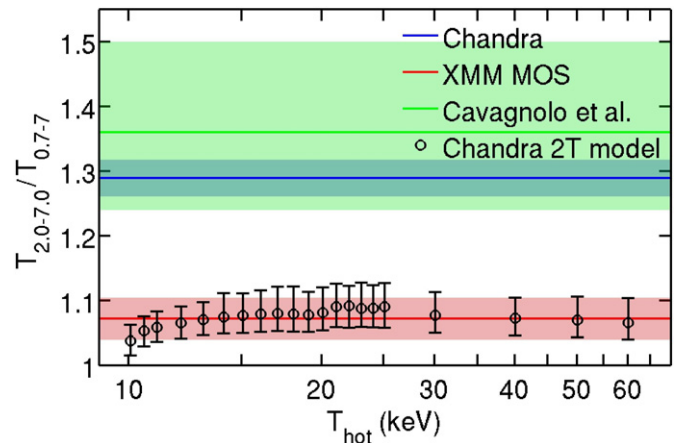### 3.3. Hard-band, Broadband Temperature

In addition to multiple-component modeling, measuring the temperature in different band-pass is another way to demonstrate the presence of multiple components. Cavagnolo et al. (2008)

---

[5] http://cxc.harvard.edu/ccw/proceedings/07_proc/presentations/david

Figure 4. Temperature of the cooler gas T_{cool}, the emission measure ratio EM_{cool}/EM_{total}, and the F-test probability P_F are plotted as a function of T_{hot}. The shaded region represents 68%, 90%, 95%, and 99% CL from 1000 simulated $T = 10.1$ keV *Chandra* spectra. The P_F from *Chandra* data without the absorption edge corrected (circles) is multiplied by 10^5.

(A color version of this figure is available in the online journal.)

reported a very high hard-band to broad-band temperature ratio for A1689, $1.36^{+0.14}_{-0.12}$, from analysis of 40 ks of *Chandra* data, suggesting that this could relate to ongoing or recent mergers. Following the convention in Cavagnolo et al. (2008), we fitted the spectrum in the 0.7–7.0 keV (broad) and 2.0/(1+z)–7.0 keV (hard) band with a single-temperature model. In contrast to C08, we do not use the $r < R_{2500}$ region with the core excised, but simply take the spectrum from the whole central 3′ (395 h^{-1} kpc) region. The hard-band to broad-band temperature ratio from *Chandra* data, 1.29 ± 0.03, strongly disagrees with that of *XMM-Newton* MOS, 1.07 ± 0.03. This result is anticipated since an absorption edge feature found in the *Chandra* spectrum (Section 2.4) is close to the cutoff of the hard band. After correcting for this absorption, the temperature ratio is in the range of 1–1.08 for an absorption depth of $\tau = 0.14$–0.10. As a consistency check, we simulated spectra according to the best-fit 2T models (from *Chandra* data) from Section 3.2 to see whether these models can explain such a high temperature ratio. Results are plotted in Figure 5. None of the 2T models can reproduce the observed ratio of the uncorrected *Chandra* data. Thus we conclude that there is no evidence from this ratio of the presence of multiple components or merging activity. Furthermore, Leccardi & Molendi (2008) do not find any discrepancy between the hard-band (2–10 keV) and broad-band (0.7–10 keV) temperature profiles, except for $r < 0.05r_{180}$, for a sample of ∼50 hot, intermediate-redshift clusters based on *XMM-Newton* observations. The high hard-band to broad-band temperature ratio seen in A1689, as well as in many other

Figure 5. Hard-band to broadband temperature ratio $T_{2.0-7.0}/T_{0.7-7.0}$ of simulated *Chandra* 2T spectra (circles) plotted against T_{hot}. The shaded regions show the observed temperature ratios from *Chandra* and *XMM-Newton* MOS data. Also shown is the temperature ratio from 40 ks *Chandra* data by Cavagnolo et al. (2008).

(A color version of this figure is available in the online journal.)
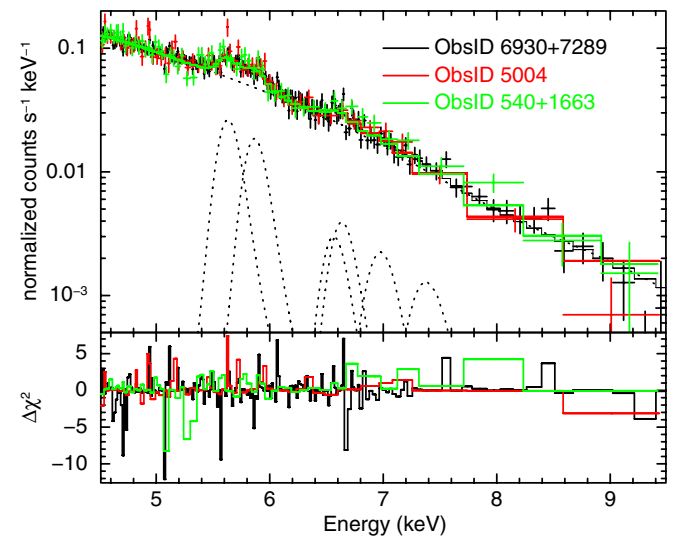
Figure 6. 4.5–9.5 keV *Chandra* spectrum of the central 3′ region. The spectrum is modeled with an absorbed thermal bremsstrahlung plus the seven Gaussian lines listed in Section 3.4.

(A color version of this figure is available in the online journal.)

clusters observed with *Chandra* (Cavagnolo et al. 2008), might be due to the aforementioned calibration uncertainty.

3.4. Emission Line Diagnostics

When fitting the whole spectrum, the temperature is mainly determined by the continuum due to the low amount of line emission at the temperature of A1689. In order to extract the emission line information, which can provide an additional temperature diagnostic, we fitted the 4.5–9.5 keV spectrum with an absorbed thermal bremsstrahlung model plus Gaussians. There are 42 lines whose emissivity is greater than 10^{-19} photons cm^{-3} s^{-1} at $kT = 10$ keV from ions of Fe xxv, Fe xxvi, Ni xxvii, Ni xxviii, according to *Chandra* ATOMDB 1.3.1. Considering the CCD energy resolution, we grouped those lines into seven Gaussians and used the emissivity-weighted centroid and one standard deviation as the line center and width, respectively. The Ni xxvii Kα line is ∼80 eV away from the Fe xxv Kβ line, not separable under CCD resolution unless
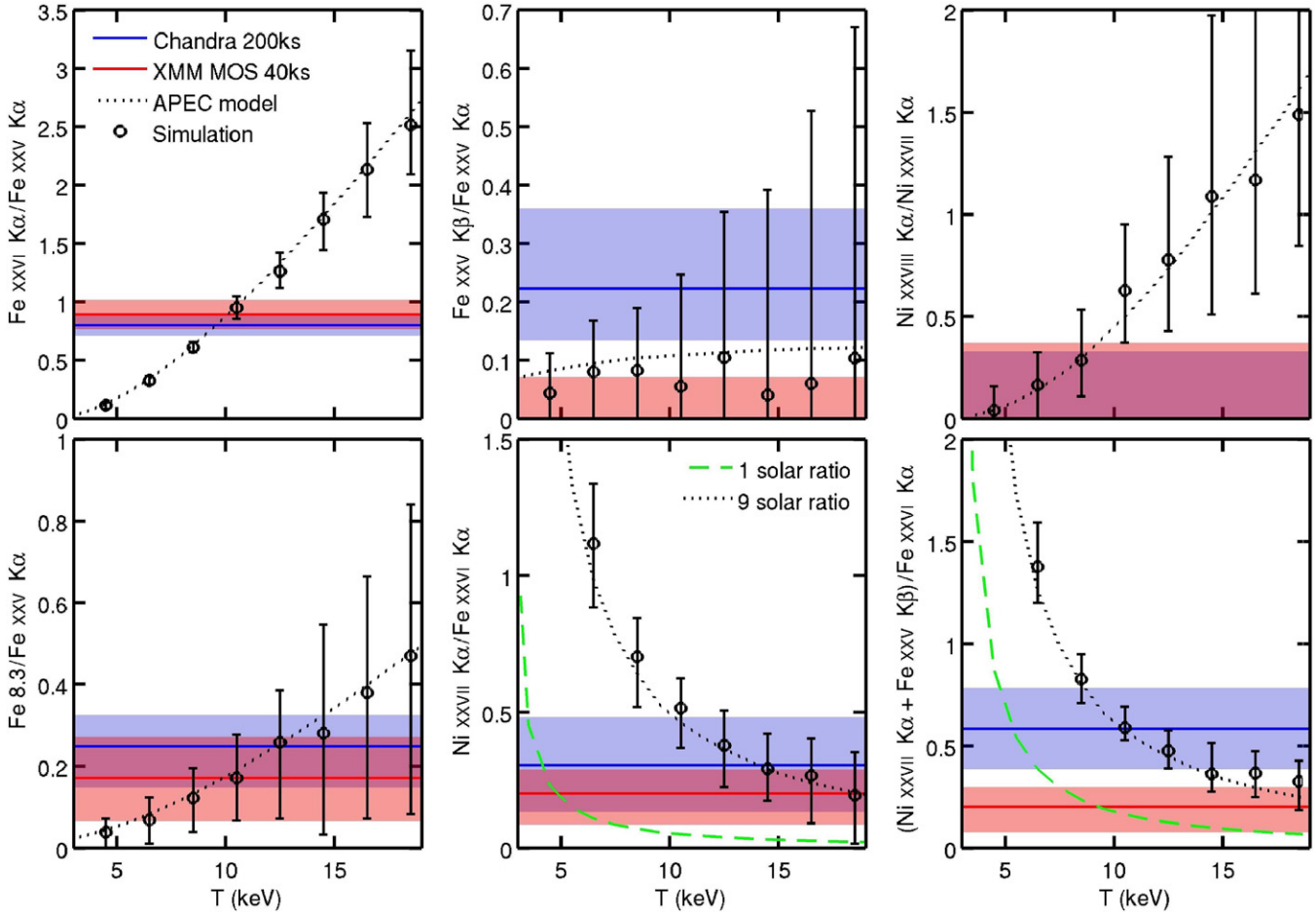
Figure 7. Predicted 1T plasma line ratio (dotted line) as a function of temperature, for various lines. The observed ratio and its 1σ confidence are shown as a solid line and shaded region. The circles show the fitted results of 100 simulated *Chandra* spectra drawn from a VAPEC model with 9 $Ni_\odot/Fe_\odot$.

(A color version of this figure is available in the online journal.)

Table 6
Modeled Emission Lines

Line	Energy (keV)	Centroid[a] (keV)	Width[a] (eV)
Fe xxv Kα	6.636, 6.668, 6.682, 6.700	6.686	23
Fe xxv Kβ	7.881	7.877	19
Fe 8.3 keV[b]	8.246, 8.252, 8.293, 8.486	8.282	68
Fe xxvi Kα	6.952, 6.973	6.964	14
Fe 8.7 keV[c]	8.698, 8.701, 8.907, 8.909	8.764	97
Ni xxvii Kα	7.765, 7.805	7.793	19
Ni xxviii Kα	8.074, 8.101	8.090	16

Notes.
[a] Emissivity-weighted center and one standard deviation. The line emissivity is calculated at $T = 10$ keV from *Chandra* ATOMDB 1.3.1.
[b] Including Fe xxvi Kβ, Fe xxv Kγ, and Fe xxv Kδ.
[c] Including Fe xxvi Kδ and Fe xxvi Kγ.

Table 7
Summary of Line Analysis

Instrument		*Chandra*	*XMM-Newton* MOS
Continuum			
T	(keV)	$10.3^{+2.2}_{-0.8}$	$9.7^{+0.8}_{-1.1}$
Emission lines			
T^a	(keV)	$9.6^{+0.5}_{-0.5}$	$10.1^{+0.7}_{-0.7}$
Ni/Fe[b†]	$(Ni_\odot/Fe_\odot)$	$8.4^{+3.7}_{-3.6}$	$1.4^{+1.8}_{-1.4}$
Ni/Fe[c†]	$(Ni_\odot/Fe_\odot)$	$5.5^{+3.2}_{-3.1}$	$3.7^{+1.6}_{-2.1}$
Fe[d†]	$(Z_\odot)$	0.31 ± 0.02	0.32 ± 0.03
Ni[e†]	$(Z_\odot)$	$1.23^{+0.50}_{-0.91}$	$1.08^{+0.52}_{-0.65}$

Notes.
[a] From Fe xxvi Kα/Fe xxv Kα.
[b] From (Ni xxvii Kα+Fe xxv Kβ)/Fe xxvi Kα.
[c] From Ni xxvii Kα/Fe xxvi Kα.
[d] From (Fe xxvi Kα+xxv Kα)/continuum.
[e] From Ni xxvii Kα/continuum.
[†] Assuming $T = 10$ keV.

we have extremely good data quality. Since we obtained an unusually high Ni/Fe ratio of ∼9 $Ni_\odot/Fe_\odot$ from a VAPEC model fitted to the whole spectrum (Section 3.1), it is worth to investigate this in detail. We therefore modeled Ni xxvii Kα and Fe xxv Kβ lines individually. Figure 6 shows the spectrum and the best-fit model. The modeled lines are listed in Table 6.

Strictly speaking, using fixed values of line centroids and widths is not correct because those quantities change with temperature. In addition, we approximated the line complex as a Gaussian whose line centroid and width calculated from

the model may not be the same after being convolved with the instrument response. To properly compare our fit results with the theory, we simulated spectra and fit them the same way we fit the real data. Figure 7 shows the observed line ratios and results from simulated VAPEC spectra with 9 $Ni_\odot/Fe_\odot$. One hundred spectra were produced at each temperature and the flux was kept at the same level as that of the data. From the good match of fitted results from simulations to the direct model
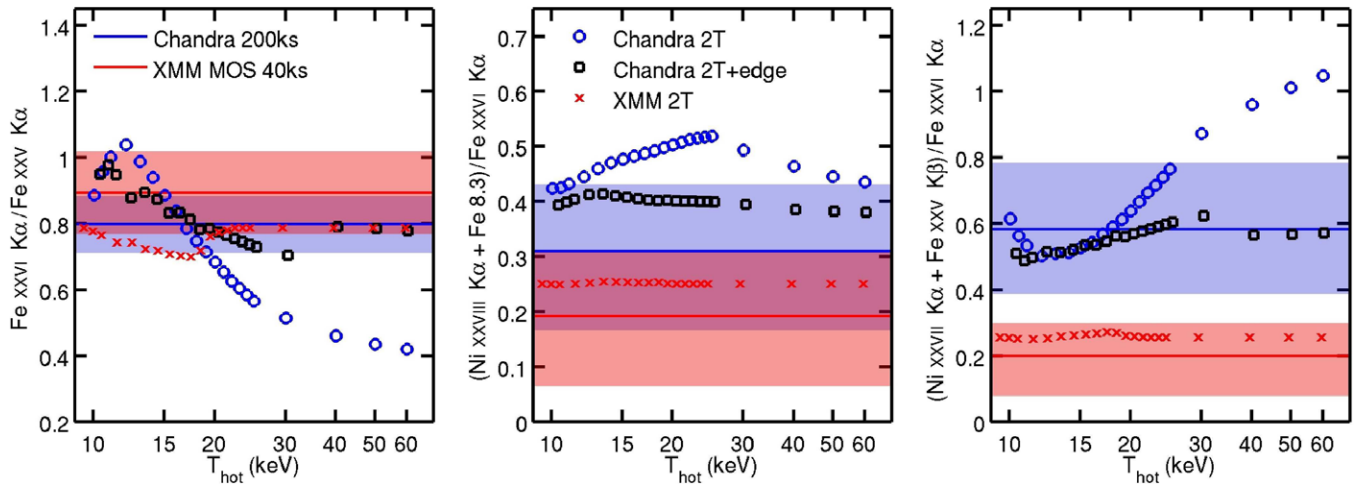
Figure 8. Predicted line ratio from the best-fit 2T (VAPEC) models (Section 3.2) as a function of the temperature of the hotter phase T_{hot}. The solid line and shaded region show the observed ratio and its 1σ error. The x-axis is in log scale.
(A color version of this figure is available in the online journal.)

prediction, we confirmed that the fitting is accurate enough to measure the line flux, though only Fe xxv Kα and Fe xxvi Kα lines are precise enough for temperature determination. Table 7 shows the temperature and abundances, inferred from a single-temperature APEC model. The iron line temperature is in very good agreement with the continuum temperature for both *Chandra* and *XMM-Newton* data. All the *Chandra* and *XMM-Newton* observed line fluxes, except Fe xxv Kβ, are consistent with each other (after an overall 9% adjustment to the flux). Using Fe xxv+Fe xxvi Kα and Ni xxvii Kα line flux, we obtain accordant Fe and Ni abundances from both instruments. The larger Fe and Ni abundances found in Section 3.1 for *Chandra* data are likely due to the higher temperature determined by the broadband spectrum and the much stronger Fe xxv Kβ line.

As discussed previously, the 2T analysis of *Chandra* data suggested that another spectral component is needed if no absorption edge modeling is applied. Figure 8 shows the line ratios predicted by the best-fit models from Section 3.2 over a wide range in temperature for the hot phase. Since the spectral energy range used in this fitting is far enough from the Si edge, it is not necessary to modify the spectral model even if the Si edge indeed needs to be corrected. The broadband *Chandra* spectrum is not sensitive to the hot phase temperature of the 2T model once it exceeds 15 keV (Figure 4). With the good constraint from the Fe xxvi Kα/Fe xxv Kα line ratio, models with $T_{hot} > 20$ keV, which are composed of great amounts of cooler gas, are rejected. Meanwhile, the ratio of higher energy states (Ni xxviii Kα, Fe xxvi Kβ, Fe xxv Kγ, Kδ) to the well-measured Fe xxvi Kα line suggests that models with lower T_{hot} are preferable.

As for the 2T models based on *Chandra* with an absorption edge model and *XMM-Newton* broadband spectra, predicted line ratios all agree with the observed value. In fact, models with $T_{hot} > 20$ keV from *XMM-Newton* data are essentially a one-temperature model, since the normalization of the hot component in these models is zero. Adding the fact that an additional temperature component does not significantly improve the χ^2 of the fit for those spectra and the remarkably good agreement on the temperature measured by the continuum and the iron lines from both *Chandra* and *XMM-Newton*, we conclude that the simple 1T model is adequate to describe the X-ray emission from the central $3'$ region of A1689.

4. DEPROJECTION ANALYSIS

Assuming that the hotter phase gas has the three-dimensional temperature profile of Lemze et al. (2008a), the radial distribution of the cooler gas can be derived. We extracted spectra from concentric annuli up to $8.'8$ ($1.2\,h^{-1}$ Mpc). The emission from each shell in three-dimensional space was modeled with an absorbed two-temperature APEC model with T_{hot} fixed at the value of Lemze et al. (2008a) and then projected by the PROJCT model in XSPEC. Because of the complexity of this model, we used coarser annular bins than those used in Lemze et al. (2008a). Data of Lemze et al. (2008a) were binned using the weighting scheme of Mazzotta et al. (2004) to produce a spectroscopic-like temperature. T_{cool}, abundance, and the normalization of both components were free to vary. The outermost two annuli were background dominated, so spectra were binned to have at least 15 net counts per bin at $r = 4.'8$–$6.'5$ (625–852 h^{-1} kpc) and 2 net counts at $r = 6.'5$–$8.'8$ (852–1161 h^{-1} kpc; see Section 2.5). Lemze et al. (2008a) predicted the gas temperature only up to 721 h^{-1} kpc, and that temperature was slightly below the observed one. Therefore, we allowed T_{hot} to change in the last two bins. The cold component was removed and the abundance was fixed at 0.2 solar in these regions in order to constrain the rest of the parameters better.

Assuming two phases in pressure equilibrium, the volume filling fraction of the ith component can be obtained from

$$f_i = \frac{\text{Norm}_i T_i^2}{\sum_j \text{Norm}_j T_j^2} \qquad (1)$$

(e.g., Sanders & Fabian 2002). Once f_i is determined, the gas density $\rho_{gi} = \mu_e m_p n_{ei}$ can be derived from

$$\text{Norm}_i = \frac{10^{-14}}{4\pi((1+z)D_A)^2} \int n_{ei} n_{Hi} f_i dV, \qquad (2)$$

where n_H/n_e and μ_e are calculated from a fully ionized plasma with the measured abundance (He abundance is primordial, and others are from Anders & Grevesse 1989). For $Z = 0.3\,Z_\odot$, $n_H/n_e = 0.852$, and $\mu_e = 1.146$. Figure 9 shows the results of this deprojected 2T analysis. The 1T modeling, in which emission from each shell has only one component, and the
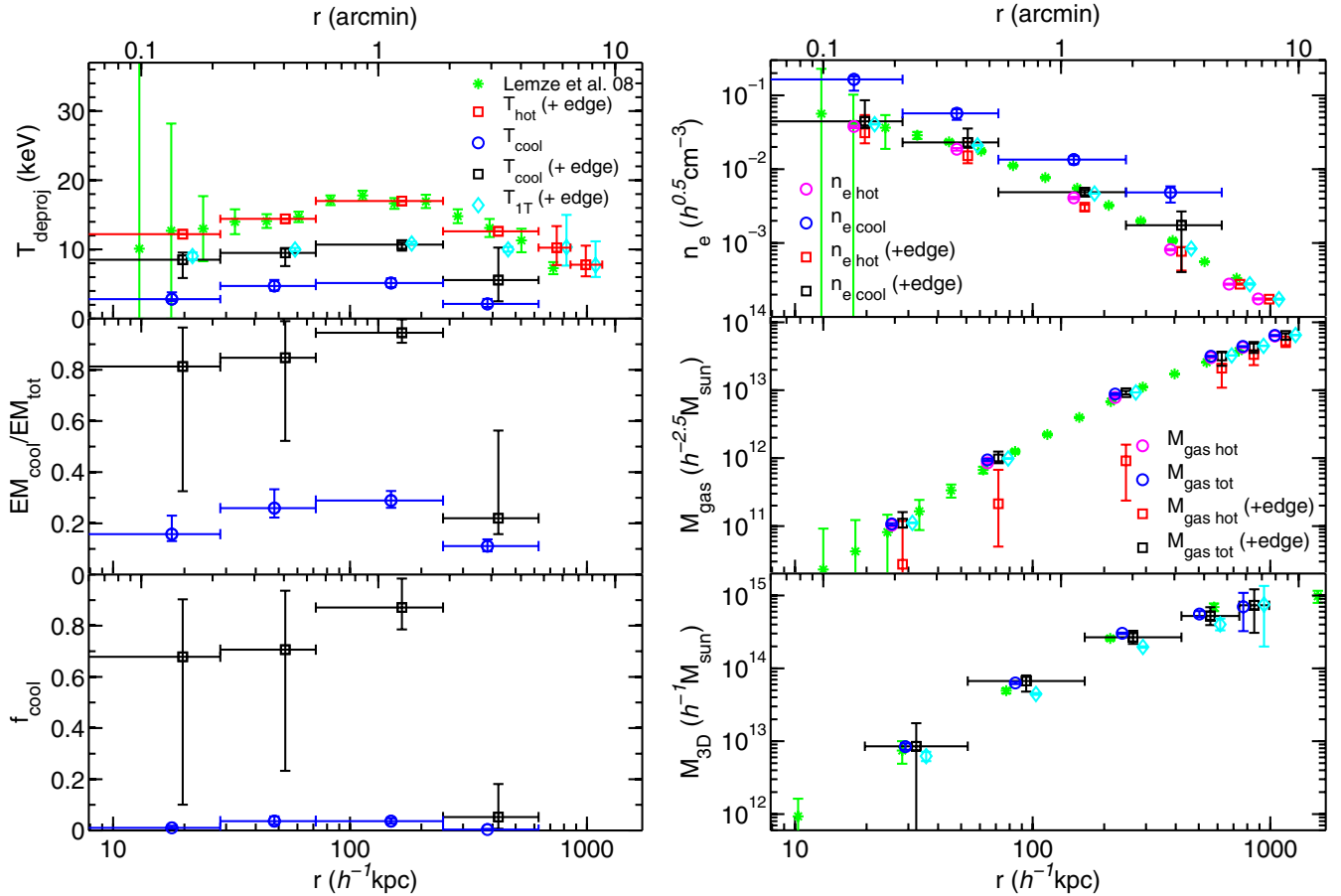
Figure 9. Temperature, emission measure ratio of the cool component EM_{cool}/EM_{tot}, volume filling fraction of the cool component f_{cool}, gas number density n_e, cumulative gas mass M_{gas}, and cumulative total mass M_{3D} profiles from the 2T deprojection analysis with an absorption edge correction (squares) and without the correction (circles). Also shown is the 1T analysis (diamonds) and results from Lemze et al. (2008a; asterisks). T_{hot} of the first four annuli was fixed at the value derived from lensing and X-ray brightness data (Lemze et al. 2008a), which were grouped into fewer bins. The cool component of the last two bins was frozen at zero. The 2T assumption is held within $625\,h^{-1}$ kpc. X-data points of the 1T and 2T models have been shifted by +10% and −10% for clarity, and their error bars are also omitted.

(A color version of this figure is available in the online journal.)

results from Lemze et al. (2008a), are also shown. If the cluster has a temperature profile of Lemze et al. (2008a), then 70%–90% of the space within $250\,h^{-1}$ kpc is occupied by the "cool" component with a temperature of ~ 10 keV, based on *Chandra* absorption edge corrected data, and this gas constitutes 90% of the total gas mass.

Kawahara et al. (2007) show that local density and temperature inhomogeneities do not correlate with each other in simulated clusters, which undermines the assumption of two phases in thermal pressure equilibrium. However, other cosmological simulations find that gas motions contribute about 5%–20% of the total pressure support (e.g., Faltenbacher et al. 2005; Rasia et al. 2006; Lau et al. 2009). If the pressure balance is off by 20%, it will not significantly change the gas mass fraction ($\lesssim 4\%$) or the volume filling fraction ($\lesssim 8\%$).

5. MASS PROFILE

Given the three-dimensional gas density and temperature profiles, the total cluster mass within a radius r can be estimated from the hydrostatic equilibrium equation (e.g., Sarazin 1988),

$$M(r) = -\frac{kT(r)\,r}{G\mu\,m_p}\left(\frac{d\ln\rho_g(r)}{d\ln r} + \frac{d\ln T(r)}{d\ln r}\right), \qquad (3)$$

for $Z = 0.3\,Z_\odot$ and $\mu = 0.596$.

If the gas has two temperatures with two phases in pressure equilibrium, the total mass still can be derived from Equation (3) with ρ_g, T replaced by $\rho_{g_{hot}}$, T_{hot}, respectively.

5.1. Nonparametric Method

To evaluate the derivatives in Equation (3), we took the differences of deprojected temperature and the gas density in log space. The radius of each annulus was assigned at $\bar{r}$ such that

$$F_{3D}(\bar{r})\frac{4\pi}{3}\left(r_{out}^3 - r_{in}^3\right) = \int_{r_{in}}^{r_{out}} F_{3D}(r)\,4\pi r^2 dr, \qquad (4)$$

where F_{3D} is the deprojected flux density from a finely binned surface brightness profile, and r_{in} (r_{out}) is the inner (outer) radius of the annulus. The radius r outside of the brackets of Equation (3) is taken at the geometric mean (i.e., the arithmetic mean in log scale) of the radii of two adjacent rings, $r = \sqrt{\bar{r}_i\,\bar{r}_{i+1}}$, and the temperature is linearly interpolated at this radius. Because errors from, e.g., T and dT/dr are not independent, standard error propagation is not easily applied. Uncertainties are estimated from the distribution of 1000 Monte Carlo simulations of T and ρ_g profiles. Figure 9 shows the total mass profile from both 1T and 2T models and the results are listed in Table 8. Two-temperature modeling, based on the T_{hot}

Table 8
Total Mass Profile

r (h^{-1} kpc)	$M_{1T+edge}$ ($10^{14}\,h^{-1}\,M_\odot$)	$M_{2T+edge}$ ($10^{14}\,h^{-1}\,M_\odot$)	M_{2T} ($10^{14}\,h^{-1}\,M_\odot$)
32^{+21}_{-13}	$0.06^{+0.01}_{-0.01}$	$0.09^{+0.09}_{-0.08}$	$0.08^{+0.01}_{-0.01}$
94^{+72}_{-41}	$0.44^{+0.01}_{-0.01}$	$0.67^{+0.13}_{-0.19}$	$0.63^{+0.02}_{-0.02}$
264^{+158}_{-99}	$1.96^{+0.04}_{-0.05}$	$2.67^{+0.60}_{-0.50}$	$3.03^{+0.06}_{-0.07}$
559^{+181}_{-137}	$4.01^{+0.80}_{-0.69}$	$5.23^{+1.67}_{-1.31}$	$5.57^{+0.53}_{-0.50}$
855^{+133}_{-115}	$7.50^{+6.04}_{-5.51}$	$7.33^{+4.84}_{-4.27}$	$7.00^{+3.88}_{-3.76}$

Notes. 2T assumption is only held within $625\,h^{-1}$ kpc. The upper and lower limits of r indicate the radii $\bar{r}$ of two contiguous rings used to calculate the mass. See the text for definitions of r and $\bar{r}$.

of L08, increases the total mass by 30%–50% for all radii within $625\,h^{-1}$ kpc. Beyond that radius, the 2T assumption is not held because of the lack of constraint on $T_{\rm hot}$.

Although the inclusion of an absorption edge in the spectral model greatly changes the derived composition of the multiphase plasma, it does not affect the mass measurement much. This is because we use a fixed $T_{\rm hot}$ profile. Once the temperature is determined, the total mass only depends on the logarithmic scale of the gas density, which produces $\sim$13% difference at most.

5.2. 1T Parametric Method

If the temperature does not vary dramatically on small scales, we can obtain a mass profile with higher spatial resolution since the gas density can be measured in detail from the X-ray surface brightness with the assumption of a certain geometry of the cluster. To achieve this, modeling of the temperature and the gas density is necessary. Following the procedure of Vikhlinin et al. (2006), we project the three-dimensional temperature and the gas density models along the line of sight and fitted with the observed projected temperature and the surface brightness profiles. A weighting method by Mazzotta et al. (2004) and Vikhlinin (2006) is used to predict a single-temperature fit to the projected multitemperature emission from the three-dimensional space. This method has been shown (Nagai et al. 2007) to accurately reproduce density and temperature profiles of simulated clusters.

The gas density model is given by

$$n_p n_e = n_0^2 \frac{(r/r_c)^{-\alpha}}{\left(1 + r^2/r_c^2\right)^{3\beta - \alpha/2}} \frac{1}{\left(1 + r^\gamma/r_s^\gamma\right)^{\varepsilon/\gamma}} + \frac{n_{02}^2}{\left(1 + r^2/r_{c2}^2\right)^{3\beta_2}}, \quad (5)$$

which originates from a β model (Cavaliere & Fusco-Femiano 1978) modified by a power-law cusp and a steepening at large radii (Vikhlinin et al. 1999). The second term describes a possible component in the center, especially for clusters with small core radius. The temperature model is given by

$$T_{\rm 3D}(r) = T_0 \frac{(r/r_{\rm cool})^{a_{\rm cool}} + T_{\rm min}/T_0}{1 + (r/r_{\rm cool})^{a_{\rm cool}}} \frac{(r/r_t)^{-a}}{(1 + (r/r_t)^b)^{c/b}}, \quad (6)$$

which is a broken power law with central cooling (Allen et al. 2001). Best-fit parameters for the gas density and temperature profiles are listed in Tables 9 and 10, respectively. Errors are estimated from the distribution of the fitted parameters of 1000
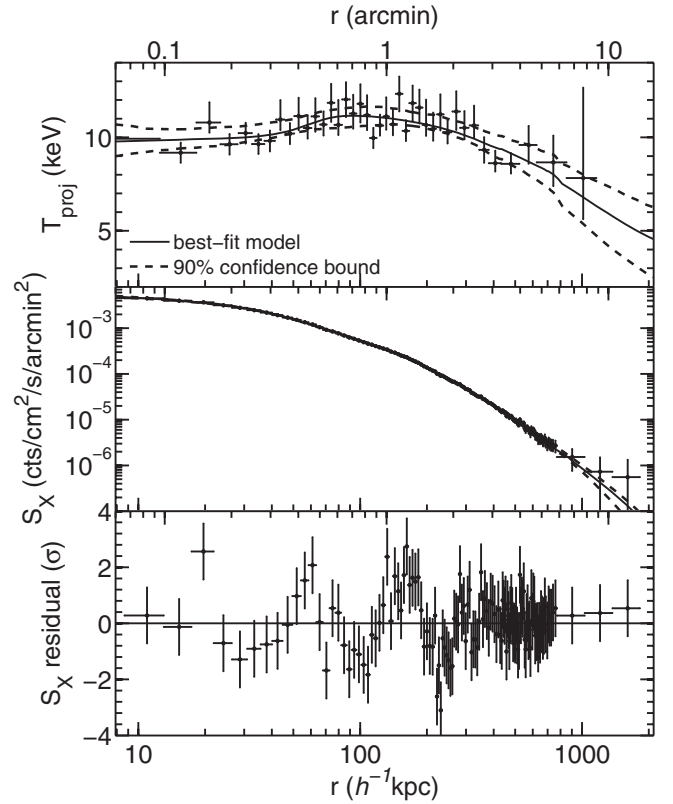
Figure 10. Projected temperature and surface brightness profiles with the best-fit model (solid lines) and its 90% confidence bounds (dashed lines). Bottom panel: residual between the surface brightness and the model. This fit gives a χ^2/dof of 154.3/155.

simulated projected temperature and surface brightness profiles generated according to the observed data and their measurement uncertainties. Since parameters are highly degenerate, some of the best-fit values are not covered by the upper or lower limits with the quoted confidence level (upper/lower bounds are for one parameter). The observed temperature and surface brightness profiles, the best-fit model, and the surface brightness residual are shown in Figure 10. The model describes the data very well (χ^2/dof = 154.3/155). The best-fit $T_{\rm 3D}$ and n_e models are shown in Figure 11. Also plotted are the profiles from the spectral deprojection fitting (Section 5.1). Compared to this nonparametric result, modeling $T_{\rm 3D}$ and n_e can avoid fluctuations from the direct spectral deprojection, which is a common problem as the deprojection tends to amplify the noise in the data (see the appendix in Sanders & Fabian 2007).

Although the second break of the first term in Equation (5) was designed to describe the steepening at $r_s > 0.3\,r_{200}$ (Vikhlinin et al. 1999, 2006; Neumann 2005), we found that if the initial guess for r_s is not big enough, r_s tends to converge to a relatively small value, $\approx$200 h^{-1} kpc, compared to the typical value of 400–3000 h^{-1} kpc for nearby relaxed clusters (Vikhlinin et al. 2006). It is possible to use the first core radius r_c or the core radius of the second component r_{c2} to account for the sharpening at 200 h^{-1} kpc. This consequently yields a more reasonable r_s at $\approx 1\,h^{-1}$ Mpc. Both cases, small (Model 1) and large (Model 2) r_s, give acceptable fits with χ^2/dof of 153.4/155 and 154.3/155, respectively. However, large r_s is harder to constrain. This makes the mass estimate more uncertain at large radii than the small r_s case.

Comparing the surface brightness profile of the northeastern (NE) part to the southwestern (SW), Riemer-Sørensen et al.

Table 9
Best-fit Parameters for the Gas Density (Equation (5))

Model	n_0 $(10^{-2}h^{\frac{1}{2}}\,\mathrm{cm}^{-3})$	r_c $(10^2\,h^{-1}\,\mathrm{kpc})$	r_s $(10^2\,h^{-1}\,\mathrm{kpc})$	α	β	ε	n_{02} $(10^{-1}h^{\frac{1}{2}}\,\mathrm{cm}^{-3})$	r_{c2} $(10^2\,h^{-1}\,\mathrm{kpc})$	β_2	γ
(1)	$3.68^{+0.01}_{-0.78}$	$0.25^{+0.10}_{-0.00}$	$1.99^{+0.19}_{-0.10}$	$0.37^{+0.32}_{-0.13}$	$0.36^{+0.04}_{-0.03}$	$1.89^{+0.24}_{-0.28}$	$0.20^{+0.03}_{-0.03}$	$2.04^{+0.26}_{-0.49}$	$7.10^{+2.54}_{-2.63}$	$4.64^{+1.23}_{-0.99}$
(2)	$0.78^{+0.14}_{-0.07}$	$1.65^{+0.11}_{-0.21}$	$11.5^{+17.4}_{+0.1}$	$1.14^{+0.08}_{-0.16}$	$0.73^{+0.02}_{-0.04}$	$0.50^{+3.66}_{-0.48}$	$0.27^{+0.03}_{-0.01}$	$1.72^{+0.16}_{-0.72}$	$6.10^{+0.85}_{-3.65}$	$2.56^{+7.06}_{-0.28}$
(3)	$2.46^{+1.08}_{-0.22}$	$0.46^{+0.03}_{-0.15}$	$2.70^{+0.19}_{-0.15}$	$0.73^{+0.09}_{-0.05}$	$0.44^{+0.02}_{-0.05}$	$1.91^{+0.36}_{-0.09}$	$0.19^{+0.02}_{-0.04}$	$2.33^{+0.14}_{-0.89}$	$10.0^{+0.0\,\mathrm{a}}_{-6.1}$	$7.52^{+0.46}_{-2.56}$
(4)	$0.64^{+0.33}_{-0.19}$	$1.98^{+0.80}_{-0.60}$	$10.2^{+27.9}_{-6.72}$	$1.20^{+0.11}_{-0.56}$	$0.77^{+0.19}_{-0.12}$	$1.45^{+2.91}_{-1.33}$	$0.27^{+0.09}_{-0.02}$	$1.77^{-0.19}_{-1.22}$	$6.01^{-0.69}_{-5.08}$	$2.08^{+8.52}_{-0.71}$

Notes. (1) Small r_s, (2) large r_s, (3) small r_s with northern clumps removed, and (4) large r_s with northern clumps removed. Errors are 95% CL for one parameter from 1000 Monte Carlo simulations. Since parameters are highly degenerate, some of the best-fit values are not covered by the upper and lower limits at this confidence level.
[a] Parameters hit the hard limit.

Table 10
Best-fit Parameters for the Temperature (Equation (6))

| Model	T_0 (keV)	$T_{\min}/T_0$	r_{cool} $(10^2\,h^{-1}\,\mathrm{kpc})$	r_t $(10^2\,h^{-1}\,\mathrm{kpc})$	a	b	c	d
(1)	$12.7^{+6.9}_{-2.8}$	$0.73^{+0.25}_{-0.34}$	$0.67^{+1.66}_{-0.29}$	$12.5^{+20.8}_{-6.8}$	$0.02^{+0.11}_{-0.14}$	$0.86^{+0.64}_{-0.36}$	$0.81^{+1.82}_{-0.40}$	$2.96^{+2.14}_{-2.45}$
(2)	$12.1^{+7.2}_{-3.4}$	$0.87^{+0.11}_{-0.41}$	$0.64^{+1.75}_{-0.15}$	$8.36^{+21.7}_{-0.93}$	$-0.02^{+0.16}_{-0.11}$	$1.37^{+0.65}_{-0.80}$	$0.89^{+2.11}_{-0.43}$	$6.78^{-0.83}_{-6.30}$
(3)	$14.4^{+5.8}_{-5.3}$	$0.40^{+0.60}_{-0.13}$	$0.77^{+1.42}_{-0.28}$	$28.6^{+0.5}_{-25.0}$	$0.11^{+0.10}_{-0.24}$	$0.40^{+1.11}_{-0.03}$	$0.59^{+1.56}_{-0.19}$	$1.44^{+3.86}_{-1.17}$
(4)	$11.8^{+8.4}_{-2.9}$	$0.86^{+0.14}_{-0.50}$	$0.74^{+1.84}_{-0.29}$	$9.08^{+23.1}_{-2.42}$	$-0.01^{+0.17}_{-0.12}$	$1.68^{+0.81}_{-1.15}$	$1.32^{+1.64}_{-0.92}$	$7.07^{-0.61}_{-6.57}$

Notes. (1) Small r_s, (2) large r_s, (3) small r_s with northern clumps removed, and (4) large r_s with northern clumps removed. Errors are 95% CL for one parameter from 1000 Monte Carlo simulations.
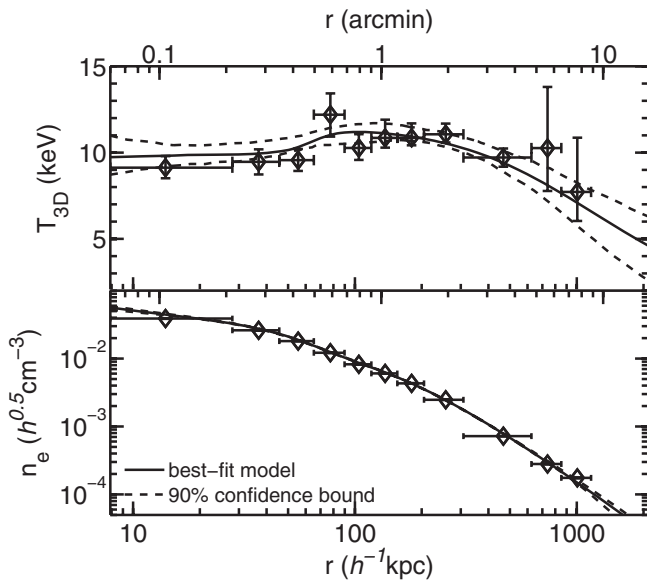
Figure 11. Best-fit T_{3D} and n_e models (solid lines) and 90% confidence bounds (dashed lines). Also shown are unparameterized results (diamonds) from Section 5.1.

Table 11
Parametric Total Mass Profile

$r\,(h^{-1}\,\mathrm{kpc})$	$M(r)\,(10^{14}\,h^{-1}\,M_\odot)$			
	(1)	(2)	(3)	(4)
32	$0.07^{+0.01}_{-0.01}$	$0.07^{+0.01}_{-0.01}$	$0.07^{+0.01}_{-0.01}$	$0.07^{+0.01}_{-0.01}$
94	$0.46^{+0.01}_{-0.02}$	$0.46^{+0.01}_{-0.03}$	$0.47^{+0.02}_{-0.02}$	$0.44^{+0.03}_{-0.02}$
264	$2.01^{+0.07}_{-0.03}$	$1.92^{+0.09}_{-0.02}$	$1.92^{+0.09}_{-0.03}$	$1.94^{+0.08}_{-0.08}$
559	$4.15^{+0.32}_{-0.02}$	$4.43^{+0.18}_{-0.11}$	$4.64^{+0.27}_{-0.03}$	$4.86^{+0.15}_{-0.51}$
855	$5.73^{+0.46}_{-0.05}$	$6.37^{+0.35}_{-0.36}$	$6.41^{+0.40}_{-0.23}$	$7.03^{+0.71}_{-1.00}$
1579	$8.60^{+0.59}_{-1.02}$	$9.52^{+2.22}_{-0.97}$	$9.85^{+0.56}_{-1.52}$	$9.55^{+3.31}_{-1.43}$

Notes. (1) Small r_s, (2) large r_s, (3) small r_s with northern clumps removed, and (4) large r_s with northern clumps removed. Errors are 68% CL from 1000 Monte Carlo simulations.

the total emission measure from another spectral component was needed in order to change the spectroscopic temperature by 1 keV. Best-fit gas density and temperature for these models are listed in Tables 9 and 10, labeled with Models 3 (small r_s) and 4 (large r_s).

The total mass profiles from these analytic gas density and temperature models are given in Table 11. We list the total mass at the radii where masses from the nonparametric method are evaluated (Table 8). The last entry of Table 11 shows the total mass at the boundary of the ACIS-I chips, $12'$ ($1.6\,h^{-1}$ Mpc $\approx r_{200}$), where S_X is detected at $\lesssim 1\sigma$. Removing asymmetric parts from the image or restricting r_s to be greater than $350\,h^{-1}$ kpc increases the total mass estimate with $\lesssim 10\%$. Nonetheless, these differences are not significant. We combine samples of the best-fit parameters of substructures removed cases (Models 3 and 4) as our best result.

Figure 12 shows a comparison of parametric and nonparametric mass profiles. The nonparametric mass profile is from a

(2009) found that the NE part is 5%–15% brighter outside $350\,h^{-1}$ kpc and 25% underluminous at $70\,h^{-1}$ kpc than the SW. To see if this asymmetry can affect the mass estimate, we fitted a symmetric model to the image and iteratively removed any part of the cluster that deviates significantly from the azimuthal mean, mainly the northern clump at $460\,h^{-1}$ kpc, the southern less luminous region at $330\,h^{-1}$ kpc, and possibly some point sources not completely removed beforehand. We did not exclude these regions from our temperature measurement since they were unlikely to bias the average temperature much for such a hot cluster, as shown in Figure 4 that at least 10%–20% of

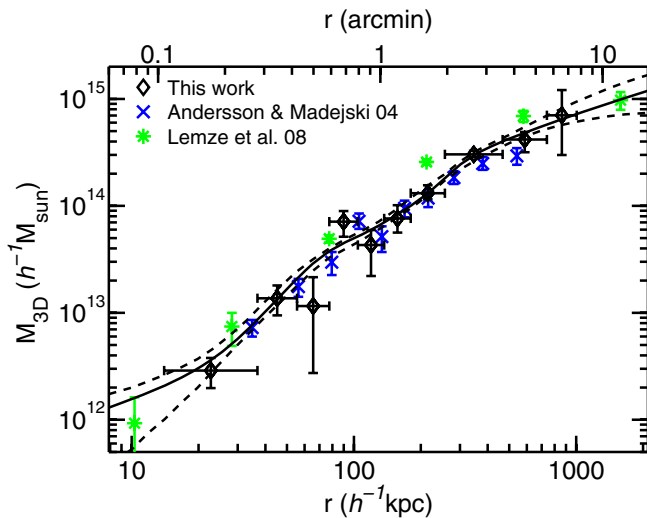**Figure 12.** Parametric mass profile (solid line) compared to the unparameterized result (diamonds). Dashed lines show the 95% confidence bounds. Also shown are *XMM-Newton* result from Andersson & Madejski (2004; crosses) and combined X-ray, strong and weak lensing analysis of Lemze et al. (2008a; asterisks). The mass profile of Lemze et al. (2008a) is mainly determined by the lensing data.

(A color version of this figure is available in the online journal.)

Figure 13. Surface mass density profiles from nonparametric (open diamonds) and parametric X-ray model (solid and dashed lines, 95% CL), compared to *HST*/ACS strong lensing analysis of Broadhurst et al. (2005b) (triangles), and combined Subaru distortion and depletion data by Umetsu & Broadhurst (2008), based on a maximum entropy method (circles). Filled diamonds show the mass from the nonparametric T_{3D} and n_e profiles that include estimations from the parametric result at $1''$ ($2\,h^{-1}$ kpc) and $13'$ ($1.7\,h^{-1}$ Mpc).

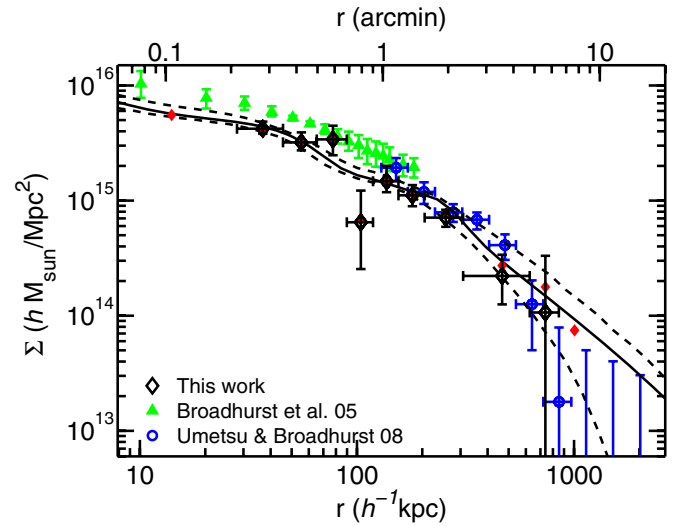(A color version of this figure is available in the online journal.)

more finely binned deprojected data than those shown in Figure 9. Results from these two methods are fully consistent with each other, although their errors are quite different. For the nonparametric method, we simply assign the observable, e.g., dT/dr, at a certain radius, so the uncertainty associated with the position is not included in the error on the mass, σ_M, but separately shown on the radius. Therefore, σ_M appears smaller if data are binned more coarsely. For the parametric method, the dependency of σ_M on the data binning is weaker. The departure from the model for any data point is assumed to be random noise and is filtered out through the fitting. Hence, σ_M reflects only the uncertainty of the fitted function and it depends strongly on the modeling.

5.3. Comparison with Other Studies

The total mass profiles of Andersson & Madejski (2004), based on *XMM-Newton*, and Lemze et al. (2008a), a joint X-ray, strong and weak lensing study are also shown in Figure 12. Our result is in good agreement with Andersson & Madejski (2004), but disagrees with Lemze et al. (2008a) around $\sim 200\,h^{-1}$ kpc. To compare our mass estimate with other lensing works, we derived the total mass density and integrated it along the line of sight. The total mass density, ρ, is obtained through the hydrostatic equation,

$$4\pi G\rho = -\frac{k}{\mu_g m_p}(\nabla^2 T + T\nabla^2\ln\rho_g + \nabla\ln\rho_g \cdot \nabla T). \quad (7)$$

For the nonparametric method, we evaluated Equation (7) in a similar fashion as we did in Section 5.1. Errors were estimated from the Monte Carlo simulations of deprojected T and ρ_g profiles. Figure 13 shows the surface mass density profiles from both parametric and nonparametric methods, along with the *HST*/ACS strong lensing analysis of Broadhurst et al. (2005b), and the combined Subaru distortion and depletion data by Umetsu & Broadhurst (2008). Since it requires at least three points to calculate the second derivative, ρ at the boundary is unknown. This will introduce additional systematic errors

to the inner and the outer projected profile. To demonstrate how this may affect our nonparametric result, we insert two artificial points at $1''$ ($2\,h^{-1}$ kpc) and $13'$ ($1.7\,h^{-1}$ Mpc) to the nonparametric T and ρ_g profiles with their values estimated from the parametric model. The projected density derived this way is shown in red filled diamonds in Figure 13. The X-ray data are consistent with those from the weak lensing, but disagree with the strong lensing analysis. Although the nonparametric data appear to agree with the strong lensing estimate at $r = 80\,h^{-1}$ kpc, this is probably due to the temperature fluctuation mentioned in Section 5.2.

The mass discrepancy is manifested when comparing the cumulative projected mass profiles, M_{2D}, shown in Figure 14. The weak lensing M_{2D} profile of Umetsu & Broadhurst (2008) includes the integration of the data of Broadhurst et al. (2005b) in the inner region. Uncertainties are from Monte Carlo simulations of the convergence profiles. The last three data points of Umetsu & Broadhurst (2008; 1–$2.3\,h^{-1}$ Mpc) are discarded since only the upper limits are available. Also shown are parametric strong lensing profiles (Halkola et al. 2006; Limousin et al. 2007), and other X-ray analyses (A04; Riemer-Sørensen et al. 2009). To convert M_{3D} to M_{2D}, Andersson & Madejski (2004) assume that the last data point reached the cluster mass limit, which unavoidably leads to underestimations especially at large radii. Riemer-Sørensen et al. (2009) use only the SE part of the cluster and four of the *Chandra* observations (excluding ObsID 540) and derive M_{2D} based on a best-fit Navarro–Frenk–White (NFW) model fitted to the M_{3D} profile. Their mass profile is generally lower than our estimate at most radii. This is contradictory to most findings that claim that the hydrostatic mass is underestimated in unrelaxed systems (e.g., Jeltema et al. 2008). Using such reasoning, and removing the NE part, presumably disturbed according to Riemer-Sørensen et al. (2009), should increase the overall mass estimate. The X-ray M_{2D} is 25%–40% lower than that of lensing within $200\,h^{-1}$ kpc, corresponding to a $\sim 1.4 \times 10^{14}\,h^{-1}\,M_\odot$ difference in the total projected mass.

Table 12
Comparison of Best-fit NFW Parameters

| Method	Instrument	M_{200} $(10^{15}\ h^{-1}\ M_\odot)$	c_{200}	χ^2/dof	Reference
Spherical model					
X-ray (1T+edge)	*Chandra*	$1.16^{+0.45}_{-0.27}$	$5.3^{+1.3}_{-1.2}$	6.3/8	This work
X-ray (parameterized $T_{3\mathrm{D}}$, n_e)	*Chandra*	$0.94^{+0.11}_{-0.06}$	$6.6^{+0.4}_{-0.4}$		This work
X-ray (2T[a])	*Chandra*	$1.45^{+0.36}_{-0.25}$	$7.6^{+1.3}_{-1.2}$	2.2/3	This work
X-ray (2T[a]+edge)	*Chandra*	$1.12^{+0.53}_{-0.29}$	$9.3^{+0.7}_{-2.8}$	0.1/3	This work
X-ray (1T)	*XMM-Newton*	0.63 ± 0.36	$7.6^{+1.7}_{-2.6}$	7.6/8	Andersson & Madejski (2004)
X-ray (1T)	*Chandra*	0.55	10.1[d]	1.6/13	Riemer-Sørensen et al. (2009)
SL	ACS	2.29	$6.3^{+1.8}_{-1.6}$		Broadhurst et al. (2005b)
SL	ACS	2.16 ± 0.32	5.8 ± 0.5	0.8/11	Halkola et al. (2006)
WL	CFHT	0.97 ± 0.13	7.4 ± 1.6		Limousin et al. (2007)
WL	CFHT	0.90 ± 0.17	13.1 ± 7.5		Corless et al. (2009)
WL	Subaru	1.24 ± 0.14	$10.5^{+4.4}_{-2.6}$	332/834	Umetsu & Broadhurst (2008)
SL+WL	ACS+Subaru	1.22 ± 0.13	$10.8^{+1.1}_{-0.9}$	13.3/20	Broadhurst et al. (2005a)
SL+WL	ACS+Subaru	1.31 ± 0.11	$9.9^{+0.8}_{-0.7}$	335/846	Umetsu & Broadhurst (2008)
SL+WL+X-ray (S_X)	ACS+Subaru+*Chandra*	1.42	$9.7^{+0.8}_{-0.7}$	15.3/24	Lemze et al. (2008a)
Triaxial model					
SL+WL[b]	ACS+Subaru	$1.15^{+0.26}_{-0.45}$	$13.4^{+1.8}_{-10.2}$	378/362	Oguri et al. (2005)
WL[c]	CFHT	0.83 ± 0.16	12.0 ± 6.6		Corless et al. (2009)

Notes. See Comerford & Natarajan (2007), Umetsu & Broadhurst (2008), and Corless et al. (2009) for a more complete compilation.
[a] With T_{hot} from Lemze et al. (2008a).
[b] Under a flat prior on the axis ratios.
[c] Under a prior on the halo orientation that favors the line-of-sight direction.
[d] Converted from best-fit parameters, $\rho_0 = 7.79 \times 10^6\ M_\odot\ \mathrm{kpc}^{-3}$, $r_s = 174$ kpc ($h = 0.7$, $\Omega_m = 0.28$, and $\Omega_\lambda = 0.72$), of Riemer-Sørensen et al. (2009), not consistent with their quoted value of 5.6 since they did not adopted the commonly defined c_{200}, the concentration at r_{200} where the enclosed mean density is 200 times the critical density (private communication).
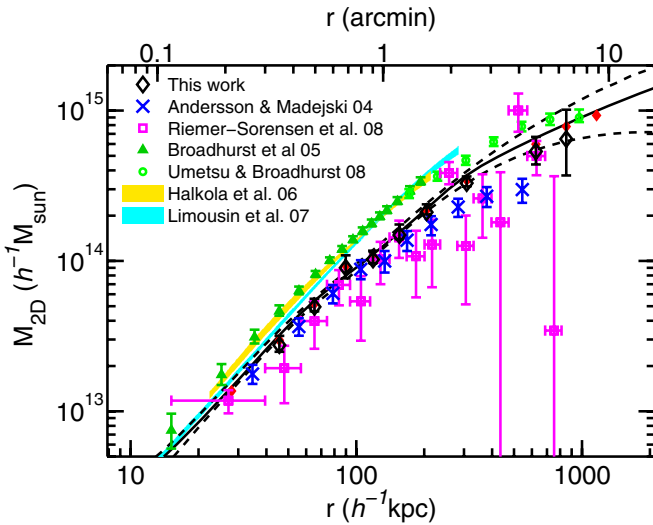
Figure 14. Projected mass profiles from nonparametric (open diamonds) and parametric analyses (solid and dashed lines, 95% CL), compared to *XMM-Newton* result from Andersson & Madejski (2004; crosses), *Chandra* result by Riemer-Sørensen et al. (2009; squares), *HST*/ACS and Subaru results by Broadhurst et al. (2005b; triangles) and Umetsu & Broadhurst (2008; circles). We integrated the lensing surface mass profile (shown in Figure 13) and estimated its uncertainties from Monte Carlo simulations. Also shown are parametric strong lensing profiles of Halkola et al. (2006) and Limousin et al. (2007; shaded regions, 68% CL). Riemer-Sørensen et al. (2009) used only SW part of the X-ray data and converted $M_{3\mathrm{D}}$ to $M_{2\mathrm{D}}$ with an NFW profile. Andersson & Madejski (2004) assumed that the last data point reached the cluster mass limit. Filled diamonds, same as Figure 13.
(A color version of this figure is available in the online journal.)

5.4. NFW Profile Parameters

The total mass profile $M_{3\mathrm{D}}$ was fitted to the NFW model (Navarro et al. 1997) to obtain the mass and the concentration parameter. To fit the nonparametric data, we weighted each point according to its vertical and horizontal errors, given by

$$\sigma^2 = \sigma_M^2 + \sigma_r^2 \left(\frac{dM}{dr}\right)^2, \qquad (8)$$

where σ_r is assigned to be 68% of the width of the horizontal error bar and dM/dr is iteratively evaluated from the NFW model until it converges. In the parametric approach, an NFW model was fitted to the parameterized mass profile that evaluated only at the radii where the projected temperature was measured with errors estimated from the standard deviation of a sample of mass profiles constructed from the simulated T_{proj} and S_X profiles described in Section 5.2. We repeated this procedure for all of the mass profiles in the sample. Resulting NFW parameters were used to estimate the uncertainty.

Table 12 lists the best-fit NFW parameters, M_{200} and c_{200}, for the total mass from both methods and from other studies, all converted to the adopted cosmology. Compared to other X-ray studies, our derived M_{200} is 30%–50% higher, closer to weak lensing results. The differences between our NFW parameters and those of Andersson & Madejski (2004) from *XMM-Newton* are primarily attributed to their slightly lower but yet consistent mass at the last data point (Figure 12). This demonstrates that the accurate mass measurement at large radii, where systematic

errors are usually the greatest, is crucial to the determination of NFW parameters.

Our results are consistent with weak lensing measurements, but with a lower concentration than what recent weak lensing studies seem to suggest (Umetsu & Broadhurst 2008; Corless et al. 2009). When these analyses are added with strong lensing information, a very tight constraint on the concentration parameter can be obtained, giving $C_{200} = 9.9^{+0.8}_{-0.7}$ (Umetsu & Broadhurst 2008), which hardly can be reconciled with our value, $5.3^{+1.3}_{-1.2}$. However, if the gas emission is modeled with two spectral components with T_{hot} from Lemze et al. (2008a), the X-ray-derived concentration is in a closer agreement to those of combined strong and weak lensing studies, but this also implies that the majority of the gas is in the cool phase and occupies most of the intracluster space (Section 3.2).

5.5. Gas Mass Fraction

The cumulative gas fraction $f_{gas} = M_{gas}/M_{total}$, derived from our best-fit T_{3D} and n_e model, is $0.098^{+0.003}_{-0.004} h_{70}^{-1.5}$ at r_{2500} ($493^{+11}_{-10} h^{-1}$ kpc), $\sim$20% higher than what is found using *XMM-Newton* data (Andersson & Madejski 2004). In spite of this seemingly large difference, the data agree that f_{gas} does not converge at r_{2500}. Much like in the case of A1689, the low-z relaxed cluster A1413 does not have a strong cooling core and also has a steadily rising f_{gas} profile out to r_{500} (Pratt & Arnaud 2002). Comparing the f_{gas} profile of A1413 with another nearby prominent cooling core cluster, A478, Pointecouteau et al. (2004) speculate that the flatter f_{gas} profile of A478 is related to the presence of a cooling core. Our f_{2500} is 11% lower than the mean gas fraction of Allen et al. (2008) derived from 42 relaxed clusters observed with *Chandra*, but our f_{500}, $0.12 \pm 0.01 h_{70}^{-1.5}$, agrees within 1% of the M–f_{gas} relation of Vikhlinin et al. (2009).

6. DISCUSSION

Nagai et al. (2007) show that following the data analysis of Vikhlinin et al. (2006) the hydrostatic mass is underestimated by $14\% \pm 6\%$ within estimated r_{2500} for simulated clusters visually classified as "relaxed." Based on the X-ray morphology, A1689 is likely to be categorized as a relaxed cluster. The X-ray centroid is within $3''$ of the lensing and optical centers (Andersson & Madejski 2004), with a very minimal centroid shift or asymmetry (Hashimoto et al. 2007). At the X-ray estimated r_{2500} of $493 h^{-1}$ kpc, we derive an enclosed hydrostatic mass of $(4.2 \pm 0.3) \times 10^{14} h^{-1} M_\odot$, $\approx$30% lower than the lensing mass from Lemze et al. (2008a). At $r = 200 h^{-1}$ kpc, this becomes a 50% difference (see Figure 12). Such a strong bias is not seen in the relaxed cluster sample of Nagai et al. (2007), assuming that the lensing mass is unbiased, although this is not unusual for "unrelaxed" clusters, referring to those with secondary maxima, filamentary structures, or significant isophotal centroid shifts.

Table 13 shows the comparison of measured M_{500} with others derived from the M_{500}–Y_X and M_{500}–T_X relations of Vikhlinin et al. (2009), calibrated from 49 low-z and 37 high-z with $\langle z \rangle = 0.5$ clusters observed with *Chandra* and *ROSAT*. A very good agreement has been achieved between these estimates. Since the M_{500}–Y_X relation is insensitive to whether the cluster is relaxed or not (Kravtsov et al. 2006) and merging clusters tend to be cool for their mass (Mathiesen & Evrard 2001), consistency among these mass estimates indicates that A1689 is relaxed in the sense that it behaves like other "relaxed" clusters on the scaling relation.

Table 13
Comparison of M_{500}

| Method	M_{500} ($10^{14} h^{-1} M_\odot$)	r_{500} (h^{-1} Mpc)
Parameterized T_{3D}, n_e	$7.3^{+1.3}_{-0.5}$	$1.01^{+0.06}_{-0.03}$
$M_{500} - T_X^\dagger$	7.7 ± 0.2	1.03 ± 0.01
$M_{500} - Y_X^a$	$7.7^{+0.5}_{-1.2}$	$1.03^{+0.02}_{-0.06}$

Notes.
[†] Scaling relations from Vikhlinin et al. (2009) with indices fixed to self-similar theory values. Errors only reflect the measurement uncertainties. Dispersions of the relation are not included. $T_X = 10.1 \pm 0.2$ keV, measured from $r = 1'.14-7'.6$ ($\approx 0.15 r_{500} - r_{500}$).
[a] By solving Equation (14) of Vikhlinin et al. (2009). The final $Y_X = T_X \times M_{gas}$ determined at r_{500} is $(5.1^{+0.5}_{-1.2}) \times 10^{14} h^{-2.5} M_\odot$ keV.

On the other hand, projection effects, such as triaxial halos or chance alignments, always have to be taken into account when comparing projected (lensing) and three-dimensional (X-ray) mass estimates. From kinematics of about 200 galaxies in A1689, Łokas et al. (2006) suggest that there could be a few distant, possibly noninteracting, substructures superposed along the line of sight. Lemze et al. (2008b), based on a 0.5×0.5 deg^2 VLT/VIMOS spectroscopic survey from Czoske (2004) which includes $\sim$500 cluster members, disagree with this projection view. They conclude that only one identifiable substructure at +3000 km s^{-1}, $1'.5$ to the NE (the X-ray clump is at $\sim 3'.5$ NE). This background group is seen in the strong lensing mass analysis (Broadhurst et al. 2005b), but is determined not to be massive ($<$10% of the total mass in the strong lensing region). Nonetheless, the higher than usual velocity dispersion in the cluster center, $\sim$2100 km s^{-1}, indicates that the central part is quite complex (Czoske 2004). This may also imply that the halo is elongated in the line-of-sight direction, as galaxies move faster along the major axis.

For powerful strong lens systems, like A1689, halo sphericity is never a justified assumption (e.g., Hennawi et al. 2007). Oguri & Blandford (2009) show that these "superlens" clusters almost always have their major axes aligned along the line of sight, with more circular appearances in projection and $\sim$40%–60% larger concentrations than other clusters with similar masses and redshifts. Gavazzi (2005) demonstrates that using a prolate halo with axis ratio $\sim$0.4, they were able to explain the mass discrepancy between the lensing and X-ray estimates of cluster MS2137-23. This cluster has a well defined cool core (e.g., Andersson et al. 2009), thus presumably relaxed, and yet a factor of 2 difference in the mass is not lessened with a multiphase model for the core region (Arabadjis et al. 2004). In contrast, triaxial modeling not only solves the mass inconsistency, but also the high concentration problem and the misalignment between stellar and dark matter components in MS2137-23 (Gavazzi 2005).

To see how the triaxiality changes our mass measurements, we modeled T_{3D} and ρ_g with prolate profiles, by replacing r in Equations (5) and (6) with $(x^2/a^2 + y^2/b^2 + z^2/c^2)^{1/2}$, where we assumed $a = b < c$ and the major axis, z-axis, is perfectly aligned along the line of sight. Following the same analysis outlined in Section 5.2 but with different projection factors, we obtained best-fit T_{3D} and ρ_g profiles. The derived mass profiles under various axis ratios a/c are shown in Figure 15. The uncertainties on $\Sigma(r)$ and $M_{2D}(r)$ are similar to those in Figures 13 and 14. We integrated the density from $z = -4.5 h^{-1}$ Mpc to $+4.5 h^{-1}$ Mpc ($\approx 3 r_{200}$ for $a/c = 1$) for all the cases.
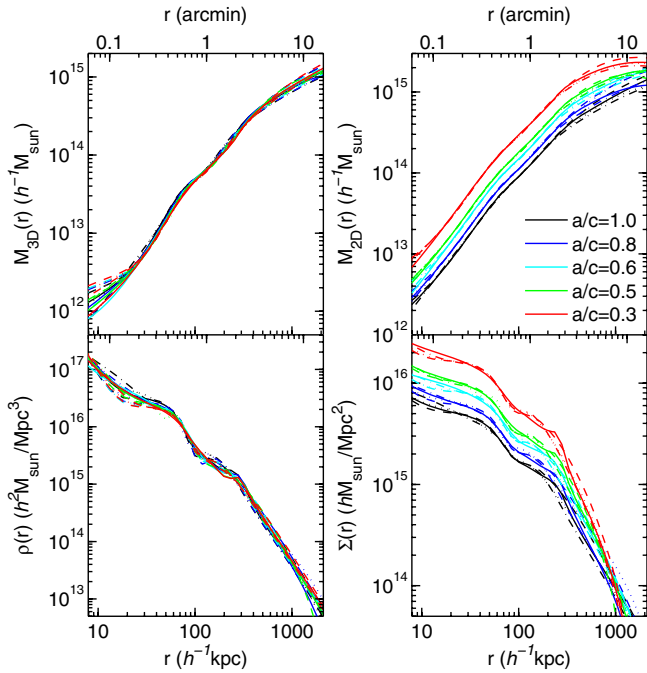
Figure 15. Best-fit mass profiles for various axis ratios *a/c* from Model 1 (dash-dotted line), 2 (dotted line), 3 (solid line), and 4 (dashed line). Top left: total mass enclosed within a sphere of radius *r*, $M_{3D}(r)$. Top right: spherically average mass density $\rho(r)$. Bottom left: azimuthally averaged surface mass density $\Sigma(r)$. Bottom right: projected mass within a cylinder of radius *r*, $M_{2D}(r)$.

(A color version of this figure is available in the online journal.)

The uncertainties of T_{3D} and ρ_g profiles at large radii ($\gtrsim 10\%$ at $r = r_{500}$ and increasing further afterward) does not significantly change the projected mass at smaller radii ($\lesssim 3\%$ within $500\,h^{-1}$ kpc).

The total mass enclosed within a sphere of radius *r*, $M_{3D}(r)$, and the spherically averaged mass density, $\rho(r)$, are basically unchanged under different assumptions of triaxiality, considering the typical measurement uncertainty. The same conclusion was drawn by Piffaretti et al. (2003) and Gavazzi (2005), though they assumed a β or an NFW model with gas isothermality. For the azimuthally averaged surface mass density $\Sigma(r)$ or the projected mass within a cylinder of radius *r*, $M_{2D}(r)$, a factor of 2 or more difference can be easily made by increasing the ellipticity. An axis ratio of 0.6, giving $M_{2D}(< 45'') = 1.4 \times 10^{14}\,h^{-1}\,M_{\odot}$ (by a factor of 1.6 increase), can resolve the central mass discrepancy, but overpredicts the mass by $\sim 40\%$ at large radii. For a ratio of 0.7, the X-ray mass estimate data agree with those of strong and weak lensing within 1% (-1σ) and 25% ($+1\sigma$), respectively. Since the gas distribution is rounder than that of the DM, a larger axis ratio than the finding of Gavazzi (2005) is expected.

Not only does the projected mass increases with the triaxiality, but also does the steepness of the profile. This explains a higher than X-ray-derived concentration from the lensing data (Section 5.4). Although some attempts have been made to model the lensing mass profile with a three-dimensional triaxial halo (Oguri et al. 2005; Corless et al. 2009), no significant constraint on the concentration parameter is obtained (Table 12). To break the degeneracy between the triaxiality and the concentration, observations from different prospective projections, such as X-ray, Sunyaev-Zel'dovich effect, or galaxy kinematics, are always needed.

Riemer-Sørensen et al. (2009) conclude that A1689 harbors a cool core based on the radial temperature profile and a hardness ratio map. From this, they conclude that A1689 is relaxed, excluding the NE half of the cluster, where there is a low mass substructure. Based on the derived temperature profile we disagree that A1689 contains a cool core. The temperature of the cluster varies radially from 9 to 11 keV with a slight drop only after $500\,h^{-1}$ kpc. This cannot be characterized as the properties of a cool core cluster. In fact, as shown in Andersson et al. (2009), A1689 is an intermediate stage cluster in terms of central baryon concentration with a minimal core temperature drop. This, does not necessarily provide evidence that the cluster is disturbed but we do not either expect the properties of a cool core cluster. Hardness-ratio maps are very sensitive to accurate background subtraction, especially for high-energy splittings. We suspect that the hardness ratio map ($S/H = E[0.3–6.0]/E[6.0–10.0]$) in Riemer-Sørensen et al. (2009), used as evidence for a cool core, suffers from residual background. The ratio decreases rapidly with radius from a central value of 2.2 and already reaches 0.4 at $3'$. This is an extremely low ratio for any reasonable cluster temperature and it is in disagreement with the observed temperature profile. For comparison, a background-free spectrum from an isothermal cluster at 10 keV would exhibit a count ratio of ~ 47 in ACIS-I given the energy bands mentioned above. The usage of unsubtracted hardness ratios in these bands shows that the high-energy band has a significant fractional background contribution and hence, is more spatially flat compared to the low-energy band. This does not provide information about the spatial distribution of gas temperatures in the intracluster medium (ICM).

7. SUMMARY

We have investigated a deep exposure of A1689 using the ACIS-I instrument aboard the *Chandra* X-ray telescope. In order to study the discrepancy of the gravitational mass from estimates from gravitational lensing, to that derived using X-ray data, we test the hypothesis of multiple temperature components in projection. The result of a two-temperature model fit shows that it is very important to take into account all details of the calibration of the instrument. We detect an additional absorption feature at 1.75 keV consistent with an absorption edge with an optical depth of 0.13. In analyzing multiple additional data sets, we find similar parameter values for this edge.

If the edge is not modeled, fitting the cluster data within $3'$ strongly favors an additional plasma component at a different temperature. However, when this absorption feature is modeled, the second component does not improve the statistic significantly and the fit results are in better agreement with the *XMM-Newton* MOS data. In all cases, a second component has to have $T > 5$ keV in order for the hot component to agree with the cluster temperature predicted by Lemze et al. (2008a) which is derived from lensing and S_X profiles. This contradicts the assertion that cool clumps are biasing the X-ray temperature measurements since these substructures would not be cool at all. We also find that, if the temperature profile of the ambient cluster gas is in fact that of Lemze et al. (2008a), the "cool clumps" would have to occupy 70%–90% of the space within 250 kpc radius, assuming that the two-temperature phases are in pressure equilibrium. In conclusion, we find the scenario proposed by Lemze et al. (2008a) unlikely.

Further studying the ratio of Fe XXVI Kα and Fe XXV Kα emission lines, we conclude that these show no signs of a multitemperature projection and the best fit of this ratio implies a

Table 14
Chandra Observation Log

Name	N_H[a]	z	ObsID	Data Mode	Obs. Date	Exp.	Background Norm.				Region	f_B[b]	S/N[c]
	$(10^{20}~\mathrm{cm}^{-2})$				(yyyy-mm-dd)	(ks)	I0	I1	I2	I3		(%)	
M87	2.59	0.00423	5826	VFAINT	2005-03-03	125.5	1.03	1.00	1.04	1.07	$6'-7\rlap{.}'5$	1.5	235
			5827	VFAINT	2005-05-05	154.4	1.10	1.09	1.09	1.13		1.5	262
			6186	VFAINT	2005-01-31	50.7	1.02	1.04	1.04	1.06		1.5	150
			7212	VFAINT	2005-11-14	64.5	1.15	1.15	1.13	1.23		1.7	168
Coma	0.89	0.0231	9714	VFAINT	2008-03-20	29.6	1.32	1.34	1.18	1.43	$< 5'$	1.9	134

Notes.
[a] Dickey & Lockman (1990).
[b] Background fraction in 1.7–2.0 keV band.
[c] Signal-to-noise ratio in 1.7–2.0 keV band.

Table 15
Absorption Edge Parameters

Name	ObsID	ccd	APEC E_{thresh} (keV)	APEC τ	APEC z	SPEX E_{thresh} (keV)	SPEX τ	SPEX z
M87	5826	0	$1.47^{+0.02}_{-0.02}$	$0.08^{+0.02}_{-0.02}$	$(4.8^{+0.5}_{-0.6}) \times 10^{-3}$	$1.47^{+0.02}_{-0.02}$	$0.10^{+0.02}_{-0.02}$	$(4.0^{+0.7}_{-0.7}) \times 10^{-3}$
		1	$1.73^{+0.02}_{-0.03}$	$0.07^{+0.02}_{-0.02}$	$(5.1^{+0.5}_{-0.5}) \times 10^{-3}$	$1.70^{+0.02}_{-0.03}$	$0.08^{+0.01}_{-0.02}$	$(4.4^{+0.4}_{-0.4}) \times 10^{-3}$
		2	$1.75^{+0.01}_{-0.02}$	$0.12^{+0.03}_{-0.02}$	$(12.8^{+0.6}_{-1.0}) \times 10^{-3}$	$1.73^{+0.01}_{-0.02}$	$0.12^{+0.02}_{-0.02}$	$(8.4^{+1.2}_{-0.3}) \times 10^{-3}$
		3	$1.79^{+0.02}_{-0.02}$	$0.09^{+0.02}_{-0.02}$	$(5.3^{+0.2}_{-0.3}) \times 10^{-3}$	$1.75^{+0.03}_{-0.02}$	$0.08^{+0.02}_{-0.02}$	$(4.5^{+0.2}_{-0.3}) \times 10^{-3}$
	5827	0	$1.75^{+0.02}_{-0.02}$	$0.11^{+0.03}_{-0.02}$	$(4.9^{+0.8}_{-0.7}) \times 10^{-3}$	$1.72^{+0.02}_{-0.01}$	$0.11^{+0.01}_{-0.02}$	$(3.8^{+1.0}_{-0.8}) \times 10^{-3}$
		1	$1.73^{+0.02}_{-0.02}$	$0.10^{+0.02}_{-0.02}$	$(5.5^{+0.5}_{-1.3}) \times 10^{-3}$	$1.72^{+0.02}_{-0.02}$	$0.09^{+0.01}_{-0.02}$	$(3.1^{+0.3}_{-0.7}) \times 10^{-3}$
		2	$1.81^{+0.02}_{-0.02}$	$0.11^{+0.03}_{-0.02}$	$(4.1^{+0.5}_{-0.2}) \times 10^{-3}$	$1.74^{+0.03}_{-0.04}$	$0.08^{+0.02}_{-0.02}$	$(2.4^{+0.3}_{-0.4}) \times 10^{-3}$
		3	$2.14^{+0.03}_{-0.04}$	$0.06^{+0.02}_{-0.02}$	$(3.8^{+0.5}_{-0.3}) \times 10^{-3}$	$2.13^{+0.04}_{-0.06}$	$0.06^{+0.02}_{-0.02}$	$(2.3^{+0.5}_{-0.3}) \times 10^{-3}$
	6186	0	$1.72^{+0.06}_{-0.06}$	$0.09^{+0.03}_{-0.05}$	$(4.6^{+0.7}_{-0.6}) \times 10^{-3}$	$1.70^{+0.04}_{-0.04}$	$0.09^{+0.02}_{-0.03}$	$(4.0^{+0.7}_{-0.7}) \times 10^{-3}$
		1	$1.73^{+0.03}_{-0.04}$	$0.11^{+0.04}_{-0.03}$	$(5.1^{+0.7}_{-0.5}) \times 10^{-3}$	$1.71^{+0.03}_{-1.71}$	$0.11^{+0.03}_{-0.03}$	$(4.4^{+0.8}_{-0.6}) \times 10^{-3}$
		2	$1.72^{+0.07}_{-0.06}$	$0.11^{+0.05}_{-0.03}$	$(8.2^{+0.5}_{-0.4}) \times 10^{-3}$	$1.66^{+0.03}_{-0.10}$	$0.10^{+0.02}_{-0.02}$	$(7.9^{+0.4}_{-0.7}) \times 10^{-3}$
		3	$1.74^{+0.03}_{-0.03}$	$0.12^{+0.03}_{-0.03}$	$(8.1^{+0.3}_{-0.4}) \times 10^{-3}$	$1.70^{+0.04}_{-0.03}$	$0.11^{+0.03}_{-0.03}$	$(7.8^{+0.3}_{-0.3}) \times 10^{-3}$
	7212	0	$1.77^{+0.03}_{-0.02}$	$0.11^{+0.02}_{-0.04}$	$(4.3^{+0.8}_{-0.6}) \times 10^{-3}$	$1.62^{+0.09}_{-1.62}$	$0.08^{+0.02}_{-0.03}$	$(1.0^{+3.4}_{-1.0}) \times 10^{-3}$
		1	$1.91^{+0.21}_{-0.05}$	$0.10^{+0.04}_{-0.04}$	$(5.8^{+0.4}_{-0.3}) \times 10^{-3}$	$2.00^{+0.04}_{-0.04}$	$0.10^{+0.03}_{-0.05}$	$(2.0^{+0.4}_{-0.4}) \times 10^{-3}$
		2	1.74_f	$0.01^{+0.03}_{-0.01}$	$(6.4^{+0.5}_{-0.7}) \times 10^{-3}$	1.74_f	$0.02^{+0.03}_{-0.02}$	$(1.2^{+1.0}_{-1.0}) \times 10^{-3}$
Coma	9714	0	$1.76^{+0.03}_{-0.02}$	$0.14^{+0.06}_{-0.02}$	$(4.6^{+0.9}_{-0.2}) \times 10^{-2}$	$1.76^{+0.03}_{-0.02}$	$0.15^{+0.04}_{-0.05}$	$(4.6^{+0.8}_{-0.2}) \times 10^{-2}$
		1	$1.75^{+0.05}_{-0.05}$	$0.08^{+0.04}_{-0.05}$	$(3.1^{+0.5}_{-0.6}) \times 10^{-2}$	$1.75^{+0.05}_{-0.05}$	$0.08^{+0.03}_{-0.05}$	$(2.6^{+0.8}_{-0.4}) \times 10^{-2}$
		2	$1.75^{+0.02}_{-0.02}$	$0.11^{+0.04}_{-0.02}$	$(3.2^{+0.7}_{-0.3}) \times 10^{-2}$	$1.75^{+0.03}_{-0.03}$	$0.10^{+0.05}_{-0.02}$	$(3.2^{+0.6}_{-0.4}) \times 10^{-2}$
		3	$1.77^{+0.02}_{-0.02}$	$0.18^{+0.03}_{-0.03}$	$(3.8^{+0.2}_{-0.4}) \times 10^{-2}$	$1.77^{+0.02}_{-0.02}$	$0.17^{+0.03}_{-0.03}$	$(3.7^{+0.3}_{-0.5}) \times 10^{-2}$
		3	$1.75^{+0.06}_{-0.06}$	$0.03^{+0.03}_{-0.02}$	$(4.8^{+0.5}_{-0.5}) \times 10^{-3}$	$1.73^{+0.05}_{-0.09}$	$0.03^{+0.02}_{-0.01}$	$(2.3^{+0.3}_{-0.8}) \times 10^{-3}$
A1689	540	13	$1.72^{+0.05}_{-0.03}$	$0.10^{+0.03}_{-0.04}$	$0.190^{+0.002}_{-0.002}$	$1.72^{+0.05}_{-0.04}$	$0.09^{+0.03}_{-0.03}$	$0.189^{+0.004}_{-0.003}$
	1663	3	$1.75^{+0.04}_{-0.03}$	$0.16^{+0.04}_{-0.03}$	$0.191^{+0.006}_{-0.011}$	$1.75^{+0.04}_{-0.03}$	$0.16^{+0.04}_{-0.04}$	$0.192^{+0.005}_{-0.012}$
	5004	3	$1.76^{+0.04}_{-0.03}$	$0.15^{+0.02}_{-0.03}$	$0.182^{+0.002}_{-0.005}$	$1.76^{+0.03}_{-0.03}$	$0.15^{+0.03}_{-0.03}$	$0.180^{+0.003}_{-0.003}$
	6930	3	$1.74^{+0.01}_{-0.02}$	$0.12^{+0.01}_{-0.01}$	$0.188^{+0.003}_{-0.003}$	$1.75^{+0.01}_{-0.01}$	$0.12^{+0.01}_{-0.01}$	$0.188^{+0.002}_{-0.002}$
	7289	3	$1.73^{+0.02}_{-0.02}$	$0.14^{+0.01}_{-0.02}$	$0.183^{+0.002}_{-0.003}$	$1.73^{+0.02}_{-0.02}$	$0.13^{+0.01}_{-0.01}$	$0.181^{+0.003}_{-0.003}$

single temperature consistent with the continuum temperatures from both *XMM-Newton* MOS and the *Chandra* data when the absorption edge is modeled.

The discrepancy between lensing and X-ray mass estimates remains, particularly in the $r < 200\,h^{-1}$ kpc region. Our X-ray mass profile shows consistent results compared to those from weak lensing (e.g., Broadhurst et al. 2005a; Limousin et al. 2007; Umetsu & Broadhurst 2008; Corless et al. 2009). Strong lensing mass profiles from different studies generally give consistent results (e.g., Broadhurst et al. 2005b; Halkola et al. 2006; Limousin et al. 2007), but none of them agrees with those derived from X-ray observations (Xue & Wu 2002; Andersson & Madejski 2004; Riemer-Sørensen et al. 2009). Using a simple ellipsoidal modeling of the cluster with the major axis along the line of sight, we find that the projected mass, as derived from the X-ray analysis, increases by a factor of 1.6 assuming an axis ratio of 0.6. We conclude that the mass discrepancy between lensing and X-ray-derived masses can be

alleviated by the line-of-sight ellipticity and that this also can explain the high concentration parameter found in this cluster.

APPENDIX

INSTRUMENTAL ABSORPTION IN *CHANDRA* DATA

To see whether the absorption feature found in A1689 (Section 2.4) is a calibration problem, we analyzed other archived *Chandra* ACIS-I observations. Objects that have high-quality data and are relatively easy to model are pulsar wind nebula G021.5-00.9, elliptical galaxy NGC 4486 (M87), and the Coma cluster. Unfortunately, due to the high galactic absorption in G021.5-00.9, it is not suitable to use those observations to verify the instrumental absorption. Details of the data sets we used are listed in Table 14. These observations have low N_H ($<3 \times 10^{20}$ cm^{-2}), low background level ($<2\%$ in 1.7–2.0 keV band), and high signal-to-noise ratios (S/Ns). Although the central part of M87 has very complex structures produced by the active galactic nucleus (e.g., Forman et al. 2007), the *XMM-Newton* observation indicates that the ICM is likely to be single phase in nature outside those regions (Matsushita et al. 2002). We extracted the spectra from $r = 6'$ to 7.5 of M87 and $r < 5'$ of Coma cluster for each ACIS-I chip and fitted with an absorbed single-temperature APEC model, multiplied by an absorption edge. The column density was fixed at the Galactic value (Dickey & Lockman 1990). The redshift and all the elemental abundances, except Al, were free to vary. Parameters for this absorption edge are listed in Table 15. For M87 whose emission is dominated by lines, these parameters are sensitive to the choice of the plasma model. Results from the latest MEKAL-based model, SPEX (version 2.0; Kaastra & Mewe 2000), are also shown in Table 15. In general, an absorption at ~1.75 keV with an optical depth of 0.1–0.15 is seen in the data sets. However, for ObsID 7212, the absorption depth is determined less than 0.05 (1σ) on ACIS-I2 and I3.

REFERENCES

Allen, S. W., Rapetti, D. A., Schmidt, R. W., Ebeling, H., Morris, R. G., & Fabian, A. C. 2008, MNRAS, 383, 879
Allen, S. W., Schmidt, R. W., & Fabian, A. C. 2001, MNRAS, 328, L37
Anders, E., & Grevesse, N. 1989, Geochim. Cosmochim. Acta, 53, 197
Andersson, K. E., & Madejski, G. M. 2004, ApJ, 607, 190
Andersson, K., Peterson, J. R., Madejski, G., & Goobar, A. 2009, ApJ, 696, 1029
Arabadjis, J. S., Bautz, M. W., & Arabadjis, G. 2004, ApJ, 617, 303
Arnaud, K. A. 1996, in ASP Conf. Ser. 101, Astronomical Data Analysis Software and Systems V, ed. G. H. Jacoby & J. Barnes (San Francisco, CA: ASP), 17
Broadhurst, T., Takada, M., Umetsu, K., Kong, X., Arimoto, N., Chiba, M., & Futamase, T. 2005a, ApJ, 619, L143
Broadhurst, T., et al. 2005b, ApJ, 621, 53
Cavagnolo, K. W., Donahue, M., Voit, G. M., & Sun, M. 2008, ApJ, 682, 821
Cavaliere, A., & Fusco-Femiano, R. 1978, A&A, 70, 677
Comerford, J. M., & Natarajan, P. 2007, MNRAS, 379, 190
Corless, V. L., King, L. J., & Clowe, D. 2009, MNRAS, 393, 1235
Czoske, O. 2004, in IAU Coll. 195, Outskirts of Galaxy Clusters: Intense Life in the Suburbs, ed. A. Diaferio (Cambridge: Cambridge Univ. Press), 183
De Luca, A., & Molendi, S. 2004, A&A, 419, 837

de Plaa, J., Werner, N., Bleeker, J. A. M., Vink, J., Kaastra, J. S., & Méndez, M. 2007, A&A, 465, 345
Dickey, J. M., & Lockman, F. J. 1990, ARA&A, 28, 215
Diego, J. M., Sandvik, H. B., Protopapas, P., Tegmark, M., Benítez, N., & Broadhurst, T. 2005, MNRAS, 362, 1247
Faltenbacher, A., Kravtsov, A. V., Nagai, D., & Gottlöber, S. 2005, MNRAS, 358, 139
Forman, W., et al. 2007, ApJ, 665, 1057
Frye, B. L., et al. 2007, ApJ, 665, 921
Gavazzi, R. 2005, A&A, 443, 793
Halkola, A., Seitz, S., & Pannella, M. 2006, MNRAS, 372, 1425
Hashimoto, Y., Böhringer, H., Henry, J. P., Hasinger, G., & Szokoly, G. 2007, A&A, 467, 485
Hennawi, J. F., Dalal, N., Bode, P., & Ostriker, J. P. 2007, ApJ, 654, 714
Iwamoto, K., Brachwitz, F., Nomoto, K., Kishimoto, N., Umeda, H., Hix, W. R., & Thielemann, F.-K. 1999, ApJS, 125, 439
Jeltema, T. E., Hallman, E. J., Burns, J. O., & Motl, P. M. 2008, ApJ, 681, 167
Kaastra, J. S., & Mewe, R. 2000, in Atomic Data Needs for X-ray Astronomy, ed. M. A. Bautista, T. R. Kallman, & A. K. Pradhan (NASA CP-2000-209968; Greenbelt, MD: NASA), 161 (http://heasarc.gsfc.nasa.gov/docs/heasarc/atomic/)
Kaastra, J. S., et al. 2004, A&A, 413, 415
Kawahara, H., Suto, Y., Kitayama, T., Sasaki, S., Shimizu, M., Rasia, E., & Dolag, K. 2007, ApJ, 659, 257
Kotov, O., & Vikhlinin, A. 2005, ApJ, 633, 781
Kravtsov, A. V., Vikhlinin, A., & Nagai, D. 2006, ApJ, 650, 128
Lau, E. T., Kravtsov, A. V., & Nagai, D. 2009, arXiv:0903.4895
Leccardi, A., & Molendi, S. 2007, A&A, 472, 21
Leccardi, A., & Molendi, S. 2008, A&A, 486, 359
Lemze, D., Barkana, R., Broadhurst, T. J., & Rephaeli, Y. 2008a, MNRAS, 386, 1092
Lemze, D., Broadhurst, T., Rephaeli, Y., Barkana, R., & Umetsu, K. 2008b, ApJ, in press (arXiv:0810.3129)
Limousin, M., et al. 2007, ApJ, 668, 643
Łokas, E. L., Prada, F., Wojtak, R., Moles, M., & Gottlöber, S. 2006, MNRAS, 366, L26
Markevitch, M., et al. 2003, ApJ, 583, 70
Mathiesen, B. F., & Evrard, A. E. 2001, ApJ, 546, 100
Matsushita, K., Belsole, E., Finoguenov, A., & Böhringer, H. 2002, A&A, 386, 77
Mazzotta, P., Rasia, E., Moscardini, L., & Tormen, G. 2004, MNRAS, 354, 10
Miralda Escude, J., & Babul, A. 1995, ApJ, 449, 18
Nagai, D., Vikhlinin, A., & Kravtsov, A. V. 2007, ApJ, 655, 98
Navarro, J. F., Frenk, C. S., & White, S. D. M. 1997, ApJ, 490, 493
Neumann, D. M. 2005, A&A, 439, 465
Nevalainen, J., Markevitch, M., & Lumb, D. 2005, ApJ, 629, 172
Oguri, M., & Blandford, R. D. 2009, MNRAS, 392, 930
Oguri, M., Takada, M., Umetsu, K., & Broadhurst, T. 2005, ApJ, 632, 841
Piffaretti, R., Jetzer, P., & Schindler, S. 2003, A&A, 398, 41
Pointecouteau, E., Arnaud, M., Kaastra, J., & de Plaa, J. 2004, A&A, 423, 33
Pratt, G. W., & Arnaud, M. 2002, A&A, 394, 375
Protassov, R., van Dyk, D. A., Connors, A., Kashyap, V. L., & Siemiginowska, A. 2002, ApJ, 571, 545
Rasia, E., et al. 2006, MNRAS, 369, 2013
Riemer-Sørensen, S., Paraficz, D., Ferreira, D. D. M., Pedersen, K., Limousin, M., & Dahle, H. 2009, ApJ, 693, 1570
Saha, P., Williams, L. L. R., & Ferreras, I. 2007, ApJ, 663, 29
Sanders, J. S., & Fabian, A. C. 2002, MNRAS, 331, 273
Sanders, J. S., & Fabian, A. C. 2007, MNRAS, 381, 1381
Sarazin, C. L. 1988, X-ray Emission from Clusters of Galaxies (Cambridge Astrophysics Series; Cambridge: Cambridge Univ. Press)
Smith, R. K., Brickhouse, N. S., Liedahl, D. A., & Raymond, J. C. 2001, ApJ, 556, L91
Snowden, S. L., Mushotzky, R. F., Kuntz, K. D., & Davis, D. S. 2008, A&A, 478, 615
Tyson, J. A., Wenk, R. A., & Valdes, F. 1990, ApJ, 349, L1
Umetsu, K., & Broadhurst, T. 2008, ApJ, 684, 177
Vikhlinin, A. 2006, ApJ, 640, 710
Vikhlinin, A., Forman, W., & Jones, C. 1999, ApJ, 525, 47
Vikhlinin, A., Kravtsov, A., Forman, W., Jones, C., Markevitch, M., Murray, S. S., & Van Speybroeck, L. 2006, ApJ, 640, 691
Vikhlinin, A., Markevitch, M., Murray, S. S., Jones, C., Forman, W., & Van Speybroeck, L. 2005, ApJ, 628, 655
Vikhlinin, A., et al. 2009, ApJ, 692, 1033
Werner, N., Durret, F., Ohashi, T., Schindler, S., & Wiersma, R. P. C. 2008, Space Sci. Rev., 134, 337
Xue, S.-J., & Wu, X.-P. 2002, ApJ, 576, 152
Zekser, K. C., et al. 2006, ApJ, 640, 639